

Structure, microstructure and disorder in low temperature chemical vapor deposited SiC coatings

H. Plaisantin^{a,b}, J. Danet^a, I. Berdoyes^c, G. Laduye^d, A. Desenfant^e, G. Chollon^{a*}

^a *Laboratoire des Composites Thermostructuraux, CNRS, Univ. Bordeaux, Safran Ceramics, CEA, 3, allée de La Boétie, 33600 Pessac, France*

^b *Safran Ceramics, 105 avenue Marcel Dassault, 33700 Mérignac, France*

^c *Dassault Aviation, 54 avenue Marcel Dassault, 33700 Mérignac, France*

^d *Air Liquide Paris, Innovation Campus, 781350 Les Loges en Josas, France,*

^e *ArianeGroup, 3 Rue de Touban, 33185 Le Haillan, France*

** Corresponding author*

Keywords: Silicon carbide; Chemical vapor deposition; Structure; Raman spectroscopy; Transmission electron microscopy

Abstract

Chemical vapor deposited SiC coatings were investigated at different scales by X-Ray diffraction, Raman microspectroscopy and transmission electron microscopy. They were prepared under specific conditions explaining the various (micro)structures obtained. The deposits all have a columnar morphology with a preferential orientation and a faulted cubic structure. They differ in how disorder is incorporated in the structure. Fine XRD analyses and stacking fault density assessment by TEM revealed the one-dimensionally-disordered (ODD) polytype in the $\langle 111 \rangle$ textured coatings. The frequency and spatial distribution of stacking faults vary and sometimes locally generate periodic alpha sequences. A specific type of disorder was also identified where $\{111\}$ planes are arranged parallel to the growth direction within the columns. These disorders, more energetic than stacking faults, induce multiple and particularly large Raman modes. Crystal distortions, such as dislocations, are localized at the ODD domain boundaries, which are frequently interrupted as they extend during the growth.

1 Introduction

Silicon carbide (SiC) coatings prepared by chemical vapor deposition (CVD) are among the best high temperature structural materials [1]. For instance, with precise control of their microstructure [2], CVD SiC monofilaments can achieve extremely high fracture strength and creep resistance [3-5]. At higher scale, SiC/SiC composites combine strength, stiffness, toughness and oxidation/corrosion resistance, making them ideal for thermo-structural applications (e.g. in future jet engines, nuclear fuel cladding...) [6]. The damage of SiC/SiC composites in operation is strongly dependent on the nature of the matrix; the reference in this field is the CVI SiC matrix, chemical vapor infiltration (CVI) being a variant of CVD for porous substrates [7]. The CVI SiC matrix is synthesized under specific conditions with respect to CVD, which are favorable to 3D fabric infiltration. Conditions of low heterogeneous reaction rates (rather at low temperature), favoring gas diffusion (at low pressure), and allowing the deposition of pure, dense and defect-free SiC are usually required. [8,9]. The microstructure of CVD and CVI SiC coatings has been studied in details since the first processing experiments [10]. During the deposition of a CVI SiC coating, at relatively low pressure and temperature, the growth rate is generally limited by heterogeneous reactions and the gas phase supersaturated [8,11]. These conditions are very different from those used for crystal growth (for example by epitaxy). They favor nucleation leading to a characteristic fine grain microstructure and a structure mostly of the β phase (*i.e.* zinc-blende, 3C in Ramsdel notation). The SiC-coatings obtained by CVI are characterized by a columnar morphology with a preferred orientation of SiC crystallites with respect to the growth direction (often $\langle 111 \rangle$) and a cubic structure containing many stacking faults [12,13]. Because of such a marked texture and imperfect structure, it is difficult to evaluate quantitative parameters to compare or classify CVD SiC deposits.

The techniques that are most often used to analyze the structure and texture of CVD SiC coatings are X-ray diffraction (XRD), Raman micro-spectroscopy (RMS) and transmission electron microscopy (TEM). XRD analysis can be carried out directly from coatings as-deposited on flat substrates. The structural analysis is then macroscopic and it can be completed by a texture analysis [14-16]. XRD is powerful for highly crystalline β -SiC coatings [14,17,18] but not very sensitive to disordered matter, especially in heterogeneous materials. This complicates the detection of possible excess phases (co-deposited free silicon or free carbon, when present, are often highly disordered), but also the analysis of structural defects in SiC, from the most energetic (*e.g.* point defects) to stacking faults. Raman spectroscopy is also helpful in identifying polytypes [19,20]. The analysis has also the advantage of being performed

at a microscopic scale. It is sensitive to the crystal orientation, in particular through polarization analyses [21]. It is also complementary to XRD, as very sensitive to free silicon and sp^2 carbon, even in a nearly amorphous form [22,23]. If phase analysis is straightforward for perfect SiC crystals, broad – but intense – bands are often observed on the Raman spectra of nanoscale or highly disordered SiC, whose analysis is complex and interpretation still subject to debate. [23-27]. TEM has two significant advantages over the other two techniques: its high spatial resolution and the direct imaging of the material, almost down to the atomic scale. At high resolution, it is the most accurate technique, via lattice fringe analysis, for investigating polytypes and stacking faults [12,28,29]. On the other hand, TEM is blind to the most disordered phases. This is the reason why these techniques are often combined for a better understanding [2,18,27,30-32], or even supplemented by more unusual ones [33,34].

However, the combination of XRD, RMS and TEM in a single study is rare. It is also uncommon to analyze, in the same study, a series of CVD SiC samples prepared under well-controlled conditions, and resulting in intentionally very different structures, textures and microstructures. Finally, it is even more unusual to correlate these characteristics with the synthesis conditions and the physicochemical processes involved during the growth.

In this study, five SiC deposits with various microstructures were prepared by CVD from two different gas precursors. For both precursors, one of the deposits was elaborated under conditions (temperature, pressure, initial gas composition, residence time) allowing to obtain a “regular” CVD SiC microstructure [12,13], *i.e.* with faulted β -SiC columns, $\langle 111 \rangle$ textured, and without secondary phase. In a second step, the CVD parameters were modified to obtain “atypical” microstructures. The analyses using each technique have allowed us to characterize the two regular deposits in details and identify the structural and microstructural modifications in the atypical coatings resulting from the alterations of the initial CVD parameters. The results of three techniques have been combined in order to make a consistent interpretation, and identify the most relevant contributions for each of them.

2 Experimental

2.1 Synthesis of the coatings

The two gas systems used to deposit the coatings are two alternative SiC precursors to the conventional methyltrichlorosilane/dihydrogen (CH_3SiCl_3/H_2) mixture [7-11,13,14,16,17,32,35]: (i) trichlorosilane/propane/dihydrogen ($HSiCl_3/C_3H_8/H_2$) [36] and (ii) methylsilane/argon (CH_3SiH_3/Ar) [37]. Trichlorosilane ($\geq 99\%$, from Sigma Aldrich) was

evaporated from the liquid phase and mixed with H₂ and C₃H₈ (respectively $\geq 99.9999\%$ and $\geq 99.5\%$, both from Air Liquide). Methylsilane ($\geq 96\%$, from Air Liquide) was supplied directly from a pressurized cylinder and mixed with Ar ($\geq 99.9999\%$, from Air Liquide). The configuration of the vertical hot-wall reactor used for both systems is described in details elsewhere [38]. The two regular CVD conditions (one for each system) were first selected to obtain a microstructure close to that required for the CVI SiC matrix. These “regular” deposits are respectively referred to as CR (HSiCl₃/C₃H₈/H₂) and MR (CH₃SiH₃/Ar). Three other coatings were prepared from the same two precursor mixtures but in different CVD conditions (*i.e.* with different initial precursor mixture, temperature or pressure), leading to well distinct microstructures. These alternate coatings are referred to as CD1, CD2 and MD. The corresponding processing parameters, *i.e.* the initial composition of the precursor mixture, temperature (T), pressure (P), duration (d) and residence time (τ_r) are specified in Table 1 (see supplementary material: SupMat 1).

	Precursor mixture	Molar ratio	T (°C)	P (kPa)	τ_r (s)	d (min)	t (μm)
CR	HSiCl ₃ /C ₃ H ₈ /H ₂	1/1/10	1070	2	0.15	75	25
MR	CH ₃ SiH ₃ /Ar	1/50	900	0.5	0.020	120	35
CD1	HSiCl ₃ /C ₃ H ₈ /H ₂	1/1.5/20	1070	2	0.16	90	25
CD2	HSiCl ₃ /C ₃ H ₈ /H ₂	1/1.5/10	900	2	0.16	150	45
MD	CH ₃ SiH ₃ /Ar	1/50	850	0.5	0.021	120	12

Table 1: Processing parameters (τ_r is the residence time of the gases in the hot zone), duration of deposition (d) and thickness (t) of the CVD SiC coatings

The coatings were all deposited on flat and polished purified graphite substrates (2318PT from Mersen, 1.86 gcm⁻³, grain size: < 5 μm, open porosity: 7%). The thickness of the coatings ranges from 12 to 45 μm (Table 1).

2.2 Characterization of the coatings

The coatings were characterized as-deposited on flat graphite substrate by X-ray diffraction (XRD, θ/θ diffractometer Bruker D8 Advance) in the Bragg-Brentano configuration. The incident X-ray beam was obtained from a copper anode ($\lambda_{\text{CuK}\alpha 1}/\lambda_{\text{CuK}\alpha 2} = 0.15405 / 0.15443$ nm). In order to keep the analyzed volume of SiC constant, an automatic/variable slit was used behind the X ray tube. The XRD patterns were acquired on a 2θ range of 10-90°. The

instrumental broadening in this configuration was 0.061° . The volume probed by XRD is significantly larger than in the case of the other two techniques. For β -SiC (density 3.2 g.cm^{-3}), at $\theta = 17.8^\circ$ (on the (111) diffraction peak), 99 % of the X-ray detected come from the first $48 \mu\text{m}$ from the surface. As all the deposit thicknesses measured by SEM are $45 \mu\text{m}$ or less, the entire thickness of the CVD SiC layers is probed by XRD.

The Raman analyses were performed with a Labram HR (Jobin Yvon) micro-spectrometer ($\lambda = 632.8 \text{ nm}$, spectral resolution $\approx 2 \text{ cm}^{-1}$, lateral resolution $\approx 1 \mu\text{m}$). Besides phase identification, the influence of polarization was examined for texture analysis of the CVD SiC coatings. The incident laser light, propagating along the X axis of the laboratory, was in all cases plane polarized along the Y axis, oriented vertically with respect to cross-section being analyzed. The different coatings were analyzed from carefully polished (down to the $1 \mu\text{m}$ grade) cross-sections parallel to the growth direction (perpendicular to their free surface). The growth direction, which is thus perpendicular to the light propagation direction, was oriented either parallel to the Y axis (as denoted by Y in bold) or parallel to the Z axis (Z). For the two different orientations, the specimen was simply rotated of an angle $\pi/2$ around the X axis of the laser, taking care to analyze exactly the same area (Table 2).

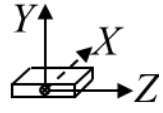
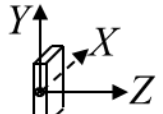
Coating orientation		Light polarization				Analysis configuration
		Incident		Scattered		
Y		Y	\updownarrow	Y	\updownarrow	YYY
		Y	\updownarrow	Z	\leftrightarrow	YYZ
Z		Y	\updownarrow	Y	\updownarrow	YZY
		Y	\updownarrow	Z	\leftrightarrow	YZZ

Table 2: Configuration of the coatings and light polarization during the polarized Raman analyses

The back-scattered light was analyzed with or without a rotating polarizer (analyzer). Two scattering arrangements were used in the former case: (i) the polarization of scattered light was set either parallel to the Y axis or along the Z axis. These different polarization/specimen orientation arrangements are denoted for instance by $\langle YYZ \rangle$, where the three terms in brackets correspond successively to the incident light polarization direction (Y), the growth direction of

the coating (**Y** or **Z** in bold) and the scattered light polarization direction (*Y* or *Z*) when the analyzer was installed (Table 2). The experiment is represented by $\langle YY(Y+Z) \rangle$ when the analyzer was not used (the whole scattered light entered the spectrometer). This procedure was validated by checking the selection rules, in the different configurations, of a 6H single crystal analyzed from a cross-section parallel to the *c* axis (the light propagation direction being perpendicular to the *c* axis). The *c* axis was oriented either along the *Y* axis or along the *Z* axis, as referred to as **Y** and **Z** respectively.

The samples for transmission electron microscopy (TEM) observations were first prepared by cutting the coatings into cross sections and thinning the slices to 120 μm by mechanical polishing with a 15 μm grade diamond plate. An ion slicer device (JEOL EM-09100IS) was then used for Ar^+ ion milling, with an incident energy of 5.5 kV and incident angle of 0.5° until 2 hours, and 2.5° until perforation of the specimen. The thin slices were then decontaminated at 2 kV for 10 minutes. The observations were all performed in the upper part of the coating (see supplementary material: SupMat 2). Low magnification observations allow to confirm that the microstructures analyzed at the top of coating are representative of the bulk material and can therefore be compared with those deduced from Raman and XRD analyses.

TEM analyses were carried out with a Philips CM30ST microscope (LaB₆ cathode, operated at 300 kV), with resolution of 0.2 nm. Conventional bright field (BF) and dark field (DF) images, as well as selected area diffraction (SAD) patterns (with a selected area diaphragm of 400 nm) were acquired from the samples. The SAD patterns were indexed with the support of Carine 3.1. software. The DF images, obtained from the 111 diffraction spot of $\beta\text{-SiC}$, were used to determine the column width (CW) from about ten measurements. CW is expressed as a range of values (minimum and maximum) in nanometers.

High-resolution TEM (HRTEM) images were obtained from the thinner parts of the thin slices with a 30 μm diameter objective diaphragm. The HRTEM images were used to calculate the stacking faults density (SFD). The number of contrast lines was determined by counting peaks of the intensity profiles along on a length of the crystal of 20 to 30 nm (see section 3.3) [39]. The SFD parameter is the average value of three measurements in different parts of the coating; it is expressed as a number of stacking faults (SFs) per nanometer (in nm^{-1} , the distance between two SFs being a multiple of 0.252 nm or approximately). The filtered details of the HRTEM images were obtained by superimposing the experimental image and the inverse fast Fourier

transform (IFFT), on which a mask filtering was previously applied to select the 111 frequencies.

All the images and patterns are formatted with the Digital Micrograph 2.31 Gatan Microscopy Suite software after scanning the negative films.

3 Results and discussion

3.1 X ray diffraction

The XRD patterns of the different coatings, with normalized intensity of the strongest peak, are compared in the [supplementary material \(SupMat 3\)](#). Except for the weak component at the left bottom of the (111) peak ($2\theta = 33-35^\circ$) related to the SF features (to be discussed below), all the 2θ positions of the SiC peaks correspond to the β phase. Several approaches have been explored to get further information on the crystallite size and the nature of the structural defects from the XRD patterns [40-44]. The main difficulties encountered in these analyses are due to peaks overlap related to different polytypes and SFs. XRD analysis of flat coatings is useful for texture analysis [14,16-18,45-47] but textured materials introduce an additional difficulty in analyzing the structure in detail. For all these reasons a Rietveld refinement (e.g. as in [44]) was not attempted. As Gosset *et al.* did for nanocrystalline SiC fibers [43], each peak was analyzed independently. Each SiC diffraction peak was refined by a pseudo-Voigt function and a linear background. For the refinement of the (111) peak, one or two asymmetric functions (skewed Gaussian model) were added in order to refine the weak SF peaks to the left of the main (111) peak. To properly analyze the SiC (220) peak, an asymmetric function was also added to adjust the (113) peak due to the graphite substrate (respectively at $2\theta = 60.14^\circ$ and 59.90°). The shape parameters of this asymmetric function were fixed from a diffraction pattern recorded from an uncoated graphite sample. Based on these XRD pattern refinements, the intensity and half-maximum width (*FWHM*) of each SiC peak can be extracted. From these data, a first parameter characterizing the texture was examined: the Harris coefficient [48]. It was chosen for simplicity, although it should not be considered as a true texture degree in case of highly textured materials [49]. It is given by [equation 1](#):

$$T_{hkl} = \frac{(I_{hkl}/I_{0\ hkl})}{\frac{1}{N} \sum_{n=1}^N \frac{I_{hkl}}{I_{0\ hkl}}} \quad (1)$$

where I_{hkl} is the pseudo-Voigt intensity for the $\langle hkl \rangle$ orientation and $I_{0\ hkl}$ is the intensity for a randomly oriented powder. Hence, a T_{hkl} value greater than 1 is indicative of a $\langle hkl \rangle$ texture, and the higher this value, the stronger the $\langle hkl \rangle$ texture. The lattice planes considered for this calculation were (111), (200), (220), and (311). The texturing of the β -SiC phase in the various deposits can be directly appreciated from the T_{hkl} ratios presented in Table 3. The $\langle 111 \rangle$ texture is very strong for CR ($T_{111} = 3.78$), slightly weaker for CD1 ($T_{111} = 3.50$) and much less marked for MR ($T_{111} = 1.74$) where the $\langle 220 \rangle$ and $\langle 311 \rangle$ directions are also well represented. On the other hand, CD2 is heavily textured along the $\langle 220 \rangle$ direction ($T_{220} = 2.96$). The MD coating is the least textured of all deposits, the T_{111} , T_{220} and T_{311} ratios being all relatively balanced (Table 3). The $\langle 200 \rangle$ direction is poorly represented compared to the other three.

	$2\theta_{111}$ (°) / d_{111} (nm)	$FWHM_{111}$ (°)	T_{111}	T_{200}	T_{220}	T_{311}	$2\theta_{SF}$ (°) / d_{SF} (nm)
CR	35.60	0.15	3.8	0.0	0.0	0.2	> 34.5
	0.252						< 0.260
MR	35.60	0.12	1.7	0.2	0.9	1.2	> 33.7
	0.252						< 0.266
CD1	35.65	0.22	3.5	0.0	0.0	0.5	> 34.6
	0.252						< 0.259
CD2	35.55	0.23	0.3	0.1	3.0	0.7	> 33.6
	0.252						< 0.266
MD	35.65	0.81	1.3	0.1	1.2	1.5	> 33.7
	0.252						< 0.266

Table 3 : Position and full width at half maximum of the (111) peak, Harris texture coefficients, position of the SF peak and SF/(111) peak ratio

The structural organization, on the other hand, can be assessed by the shape of the diffraction peaks of the β phase and the occurrence of other features. The peak positions were not precisely examined because of some uncertainties related to the height and flatness of the deposits. However, the (111) peak was consistently found at $35.6 \pm 0.05^\circ$ (0.252 ± 0.0003 nm) for all specimens, as expected for β -SiC (Table 3). The peak widths ($FWHM_{111}$) was the first structural

parameter that was examined (only $FWHM_{111}$ is presented in Table 3, the other peaks being often too weak to be analyzed). The peak widths are low for both MR and CR (0.12 and 0.15°), slightly higher for CD1 and CD2 (0.22 and 0.23°), and much higher for MD (0.81°). Several effects may contribute to diffraction peak broadening in addition to that of the instrument: the size of the coherent diffracting domains (Scherrer equation), microstrains (local lattice deformations due to dislocations or other structural defects) [43,44,50], and SFs [41,42]. In contrast to Gosset et al., a Williamson and Hall analysis was not applied to the present CVD SiC coatings. As we will see in the following TEM analysis, the assumption of coherent diffracting domains (CDDs) of constant size is clearly invalid and the structural defects are too abundant and diverse in nature for the parameters deduced from this approach to be really significant. Furthermore, the effect of SFs in peak broadening is not taken into account in the latter model although it can be important compared to that of the CDD size effect [42].

The stacking fault features were therefore examined in more details. The $2\theta = 30-40^\circ$ region of the XRD diagrams showing the SFs peaks at the left bottom of the (111) peak is presented in Fig. 1. First of all, a fine and very weak peak is visible at 32.1° (0.279 nm) for CR, CD1 and MR. Although this peak does not correspond to any known polytype, disordered SiC form, or secondary phases, it was found to be characteristic of relatively well-crystallized and $\langle 111 \rangle$ -textured CVD SiC deposits. No assignment could be given at this time. More expectedly, a shoulder is visible to the left of the (111) peak for all deposits, which reflects the presence of at least one asymmetric component. This asymmetrical feature is sharp on its left side but widens on its right side, at the bottom of the (111) peak, forming a continuous background of complex shape. A similar feature was observed experimentally from SiC powder [33] or large and highly oriented columns (several micrometers wide) in CVD films deposited at high temperature [47]. A similar peak, though significantly broader, was also evidenced in SiC fibers obtained by pyrolysis of preceramic precursor [43]. This shoulder is very weak for CR, CD1 and MR, and much more intense for the low temperature CVD SiC coatings (MD and CD2), consistent with the work of Klein *et al.* [30] (Fig. 1). The position of this asymmetric peak also varies significantly depending on the deposit: it ranges $2\theta_{SF} = 34.5-34.6^\circ$ ($d_{SF} = 0.259-0.260$ nm) for CR and CD1 and $2\theta_{SF} = 33.6-33.7^\circ$ ($d_{SF} = 0.266$ nm) for MR, MD and CD2 (Fig. 1, Table 3). Using an axial next-nearest neighbor Ising (ANNNI) model [51], Pujar and Cawley simulated the XRD data resulting from a 1D stacking algorithm generating switches between fault-free domains (FFD) and faulted domains (or Ising domains, ID) [41,42]. The three simulation variables of the model are the frequency of switching from the FFD to the ID, the volume

fraction of layers within the ID, and the density of stacking faults within the ID (which is controlled by temperature, supersaturation, impurities and stresses) [41]. These authors have shown that the background intensity and profile around the (111) peak are respectively determined by the average width of the ID and the spatial distribution of stacking faults within the ID [41]. Applied to SiC CVD coatings, Pujar and Cawley's analysis tends to show that CR, CD1 and MR contain large width FFDs, because of the low background in the (111) peak region, as opposed to CD2 and MD. On the other hand, the MR coating differs from the other two deposits by its high density of intrinsic SFs (one-layer microtwins), as suggested by the high d_{SF} value (Table 3) [40]. The CD2 and MD coatings are characterized by large IDs with a high density of defects, consisting of rather extrinsic SFs (two-layer) or larger microtwins in the MD coating, as suggested by the strong (111) peak backgrounds, and rather intrinsic in CD2, as shown by the presence of a sharp 0.266 nm peak [41].

3.2 Raman micro-spectroscopy

Except the $E_1(\text{LO})$ mode (which is not observable in the back-scattering geometry) and the $A_1(\text{LO})$ mode (which is in all cases forbidden when the light propagation direction is perpendicular to the c axis), all the optical phonons characteristic of the 6H-SiC phase are clearly identified on the Raman spectra recorded for various polarizations and orientations of the SiC single crystal (see [supplementary material: SupMat. 4](#)): $E_{2\text{low}}$ at 767 cm^{-1} , $E_{2\text{high}}$ and $A_1(\text{TO})$ at 789 cm^{-1} , $E_1(\text{TO})$ at 798 cm^{-1} [20,52,53]. The peaks are all very sharp ($\approx 3\text{ cm}^{-1}$ in width), typical of a perfect crystalline state. The selection rules are also strictly observed, validating the sample preparation and the polarization analysis procedure. Indeed, as expected, the two E_2 modes are allowed only for the YZY configuration, $A_1(\text{TO})$ for both YYY and YZY , and $E_1(\text{TO})$ for both YYZ and YZZ [21,52,53].

The spectra of the various CVD SiC coatings are first compared in the same $YY(Y+Z)$ configuration to highlight the possible phases present and evaluate the organization state of silicon carbide (Fig. 2). Except for the CD1 coating, all spectra exhibit only typical silicon carbide features. The CD1 specimen indeed contains traces of highly disordered free sp^2 carbon, as shown by the presence of broad and overlapping D and G bands at 1350 and 1600 cm^{-1} [54,55] (only the low-frequency region of the D band is visible on the spectrum shown in Fig. 2). The SiC Raman features vary significantly for the different coatings, especially in terms of bandwidth of the optical phonons visible in the range $650\text{-}1000\text{ cm}^{-1}$. Relatively sharp and

intense TO and LO components appear for the CR, MR and CD1 specimens, in the range 730-820 cm^{-1} and 950-990 cm^{-1} , respectively (Figs. 2,3a-3c). On the other hand, complex acoustic modes appear below 650 cm^{-1} for all coatings, as well as broad but well distinct components in the optical phonon region. These bands, at about 700, 765, 795, 830, 885 and 935 cm^{-1} (typically 30-80 cm^{-1} in width, as determined by peak fitting), appear on all the spectra and are particularly visible for the MD and CD2 samples, which do not show narrow TO and LO peaks (Figs. 3d,3e). The latter sharp optical phonons, which show some similarities with those of β and α -SiC phases (3C, 2H, 4H, 6H, 15R...), are characteristic of the most crystalline phases in the coatings. The multiple and overlapping TO components and their large width (typically 8-30 cm^{-1}) do not support the existence of pure cubic or hexagonal polytypes. On the other hand, they cannot be explained by a simple phonon confinement effect in defect-free nanometric crystallites [23,56-57], but rather by the presence of a high density of random stacking faults. Romfeld *et al.* indeed used a bond-polarizability model [20,58] for high SF densities, which reproduces the width of the main TO phonon as well as the low frequency component at 765 cm^{-1} (that is also present on the CR, MR and CD1 spectra, see Figs. 3a-3c) [59]. For the most crystalline coatings, a detailed examination of the TO phonon region reveals three distinct peaks that appear at frequencies close to those of 6H polytype, although broader (10-12 cm^{-1}) and overlapping. Similar phonons were already observed in the 111-textured sheath of CVD SiC monofilaments, whose selection rules were similar to that of the 6H crystal [53]. The high amount of random stacking defects along the 111 axis was indeed found to induce not only new TO components, but also an axial symmetry of the coherent domains, which leads to TO phonon selection rules similar to those in the 6H phase, depending to the orientation of the crystal and the incident/scattered polarization [53].

The polarization analyses have been carried out precisely to highlight a possible preferential orientation of the crystalline domains in the deposits. The spectra of the various coatings are shown in Figs. 3a-3e for the four different configurations *YYY*, *YYZ*, *YZY* and *YZZ*. The preferential orientation is obvious in the case of the CR and CD1 deposits: the intensity of the three narrow TO components vary significantly with the polarization/orientation configuration. Moreover, the three phonons follow more or less strictly, depending on the deposit, the same selection rules as the E_2 , $A_1(\text{TO})$ and $E_1(\text{TO})$ modes for the 6H-SiC phase (see [supplementary material: SupMat. 4](#)) [52,53,60]. The narrow TO components of the MR spectrum are much less polarization sensitive than for CR and CD1 but more remarkably, only two components are visible instead of three. A peak fitting of the TO components was performed for a more accurate

comparison of the spectra of the three most crystalline coatings (CR, CD1 and MR). All the spectra evidence two common components at 768 ± 2 and 798 ± 1 cm^{-1} , analogous respectively to the $E_{2\text{low}}$ and $E_1(\text{TO})$ peaks of 6H-SiC (respectively at 767 and 797.9 cm^{-1} [19,52]) in terms of selection rules. A third more intense component is also observed between the two previous ones, which is located at 786 and 788 cm^{-1} respectively for CR and CD1. This intermediate peak, equivalent to the $A_1(\text{TO})/E_{2\text{high}}$ modes in 6H-SiC (789 cm^{-1} [19,52]), is shifted at 794 cm^{-1} for the MR coating (close to the $E_1(\text{TO})$ peak). Furthermore, it does not obey the selection rules expected for the hexagonal symmetry, contrary to the case of the two other coatings (Fig. 3c). Feldman *et al.* correlated the $\Delta\text{TO} = \text{TO}_1 - \text{TO}_2$ peak splitting (here $E_1(\text{TO}) - A_1(\text{TO})/E_{2\text{high}}$) with the percentage of “hexagonal” layers (or microtwins) in the polytype stacking sequence [19,52]. Shatwell *et al.* applied the same analysis to heavily faulted CVD SiC coatings [2,61], in which the stacking sequence is random instead of periodic in the polytypes [58]. The ΔTO peak splitting values obtained for CR, CD1 and MR, of respectively 12, 10 and 2 (± 2) cm^{-1} , correspond to a hexagonal character of about 40, 33 and 7 (± 7) %. This results indicates that the density of random SFs in the 3C structure (*i.e.* the hexagonal character) is slightly higher for CR than for CD1, and very limited in MR. The strong cubic character of the latter is also probably related to the lower sensitivity of the TO peaks to the polarization configuration and orientation of the coating. Even assuming a preferential orientation of the crystallites in the 111 direction in this deposit, the cubic symmetry induces a much lower anisotropy of the TO peak intensity than the uniaxial symmetry of the hexagonal polytypes [21], or the faulted β -SiC structures [53], such as here in CR and CD1. The analysis of the $A_1(\text{LO})$ phonon, on the other hand, does not bring additional information on the structure and texture of the different deposits. This mode is forbidden for all polarizations and orientations of a 6H-SiC crystal when the light propagation direction is perpendicular to the c axis. It is also considerably attenuated for faulted CVD SiC coatings showing a strong preferential orientation of the crystallites along the 111 direction, when the propagation direction is perpendicular to the growth direction [2,53,60-62]. Given the above results on the TO phonons (showing the 111 texturing in the CR and CD1 deposits), the intensity of the $A_1(\text{LO})$ mode can thus be related to the degree of disorientation of the 111 crystallite axis with respect to the growth direction.

The origin of the broad but distinct components, little affected by polarization/orientation, and visible especially for MD and CD2 (Figs. 3d,3e), is more uncertain. However, it seems reasonable to assume that they are associated with the highest energy structural defects, which are present in the most disordered part of the SiC phase, and particularly abundant in MD and

CD2. Similar features were observed for other disordered SiC-CVD coatings and nanorods [24-26,63]. Interestingly, the authors evidenced that the appearance of the spectra was significantly altered by changing the excitation wavelength and, more precisely, that a longer wavelength ($\lambda = 633$ nm or higher) lead to features that are much broader, more intense between the TO and LO modes, near the LO region [25,26,63], and even sometimes new around 700 cm^{-1} (*i.e.* outside the TO-LO domain) [26], similar to those observed here. This effect cannot be related to changes in the probed depth (for highly crystalline CVD SiC, it has been experimentally estimated around $0.75\pm 0.25\text{ }\mu\text{m}$ at $\lambda = 633$ nm: see [supplementary material: SupMat 5](#)) : an opposite result would be expected if surface defects were created during sample preparation. The new broad bands in the LO region and the red shift and broadening of the LO mode are rather the consequence of a resonance effect induced by Fröhlich electron-phonon interaction, a phenomenon that depends on the band gap energy of the material and the incident light energy [24-26,63]. In the disordered CVD SiC coatings, these so-called surface or interface modes (IF) can be assigned to high energy defects, probably concentrated at the grain boundary or between coherent – defect-free – domains, at smaller scale. These defects induce a break in the translational symmetry so that all the optical phonons may contribute to the first-order Raman spectra, with no expected dependence on polarization or orientation, via a Fröhlich enhanced effective density of optical phonon states [25,63].

3.3 Transmission electron microscopy

BF images of the two regular coatings (CR and MR) clearly reveal the columnar microstructure of the deposits (Fig. 4). They show important variations in contrast, indicating a relative disorientation of the columns between them and with respect to the growth direction, as well as numerous imperfections in the crystal structure. In particular, many columns show alternating lines of contrast, perpendicular to their maximum length (*i.e.* to the growth direction), as often reported for columnar CVD or CVI SiC [9,12,13,18,27,28,30,35,64]. These numerous and parallel striations are interpreted as a high density of planar defects – or SFs – in the crystal [12,65]. The overall contrast of the columns is more homogeneous in the CR coating suggesting a better crystalline organization than in the MR coating. The column width ranges from 150 to 400 nm in CR and 50 to 150 nm in MR (Fig. 4). The SAD pattern associated with a given column of the CR coating (Fig. 5a) indicates that the SiC structure is cubic, with the {111}

planes perpendicular to the main column axis. The lateral spots are degenerated into straight lines parallel to the $\langle 111 \rangle$ direction indicating that the stacking of the dense Si-C bilayers is random. This structure is usually described as a “one-dimensionally-disordered” (ODD) SiC [28]. It can be described like very thin β -SiC lamellae separated by frequent stacking faults. SFs consist of single twins or pairs of closely spaced twins (e.g. intrinsic or extrinsic faults) that appear randomly and not periodically, as in α polytypes. For the MR coating, sharp 220, 111 and 002 spots are clearly visible and the degenerated straight lines are less marked on the SAD pattern than for the CR coating (Fig. 5b). Moreover, unexpected spots, pointed by the symbol #, are identified in addition to the characteristic spots of the β structure, which could be attributed to either twinning along $\{111\}$ planes or an α polytype (a more precise identification is not possible at this stage). Regarding the diffraction pattern of Fig. 5b, it must be noted that only one of the columns included in the selected area gives rise to the complete diffraction pattern: the one that lies exactly on the $[-110]$ zone axis (possibly the most illuminated one, in the center of the dotted black circle). The other slightly misoriented columns are only related to the axial 111 spots.

The use of the lattice fringe imaging allows an accurate identification of the ODD polytypes in the SiC matrix of SiC/SiC composites elaborated by CVI [12]. Similarly, no periodicity in the stacking is detected in the HRTEM images of the CR coating (see the high magnification inset in Fig. 6a). Yet, the distance between neighboring $\{111\}$ planes (0.252 nm) is preserved in the high SF density areas, as already observed by Jepps *et al.* [29]. The distribution of SFs remains mostly random in the β -SiC structure of the MR coating (Fig. 6b). On the other hand, a few sequences of periodic stacking of the Si-C bilayers can be occasionally observed within some columns, highlighting the presence of nanodomains of a certain α polytype (see contrast lines in the high magnification inset in Fig. 6b). To complete this analysis, the IFFT of a surface area of 40 x 40 nm was carried out on the respective HRTEM images of the CR and MR deposits (see boxed areas and SAD insets in Figs. 6a,6b). The straight and diffuse lines in the CR diffraction pattern are typical of an ODD polytype. In contrast, for the MR coating, well distinct diffraction spots appear, which can be attributed to the 6H structure (in Fig. 6b, in the hexagonal system, the zone axis is 1000 and the 0001 axis is oriented vertically). The presence of such α nanosequences in the ODD polytype has already been revealed by HRTEM in CVD coatings [64].

The stacking faults can be directly highlighted via the stacking sequence of bilayers on HRTEM lattice fringe images [12, 29,39]. But the conditions of resolution and orientation of the crystal

that are necessary for their observation are only seldom met. Shinozaki *et al.* showed that the contrast lines associated with SFs, which are caused by a sudden change of the diffracted wave phase when crossing the faulted plane, can be observed under less restrictive conditions [65]. The SF density (SFD) was evaluated by counting the contrast lines visible in columnar grains, either directly, when they are not too numerous [66, 67], or by exploiting the intensity profiles across the lattice fringe sequences [39]. The same procedure was applied to the current TEM images to quantify the SFD parameter in the various CVD SiC coatings. The measurement is considered valid when the distance between two faults is close to a multiple of 0.252 nm. An average stacking fault of 1.0 nm^{-1} is estimated for CR, *i.e.* at least one fault every four Si-C bilayers. This value is particularly high compared to those obtained from epitaxial CVD SiC (*e.g.* $\approx 0.01 \text{ nm}^{-1}$, as reported in [66] and [67]). On the other hand, it is relatively close to the values expected for periodic polytypes (*e.g.* 1.3 nm^{-1} for 6H) although CR obviously belongs to the ODD type. In comparison, in some columns of the MR coating, the SFD is on average nearly half that in the CR coating (0.6 nm^{-1}). Such a low value occasionally allows the appearance of short periodic microtwin sequences, as identified on the SAD pattern (Figs. 5b,6b).

When the CVD parameters deviate from the reference conditions selected for the CR and MR coatings, major structural changes occur, which can be identified by TEM. In the CD1 coating, obtained with higher $\text{H}_2/\text{SiHCl}_3$ and $\text{C}_3\text{H}_8/\text{SiHCl}_3$ molar ratios than for CR, the columns visible from the DF imaging (Fig. 7a) are significantly thinner (from 100 to 150 nm, *vs* 150–400 nm for CR). The area selected for diffraction, with a diameter of 400 nm, then comprises several columns. The associated diffraction pattern (Fig. 7b) exhibits several 111 spots distributed over a circle of radius 3.97 nm^{-1} (0.252 nm), which indicates that the columns are slightly disoriented with respect to each other, while keeping a common $\langle 111 \rangle$ growth direction. By HRTEM imaging (Figs. 7c,7d), short and distorted fringes ($\approx 0.35 \text{ nm}$ wide) can be detected between the SiC columns, indicating the presence of turbostratic carbon nanodomains. The stacking fault density in the CD1 coating is 1.1 nm^{-1} , *i.e.* slightly higher than in CR, and the SF arrangement is random and ODD, in accordance with the striated aspect of the interior of the columns (Fig. 7d)

The microstructure of the CD2 coating, which is deposited at lower temperature and with a higher $\text{C}_3\text{H}_8/\text{SiHCl}_3$ ratios than the CR coating, can be seen in two DF images obtained from two separate columns, the former (Fig. 8a) being more representative of the coating than the latter (Fig. 8b). The corresponding SAD patterns are surprisingly punctuated (Figs. 8c,8d). The

columns are much wider than in CD1 (150–400 nm), and similar in size to those in the CR coating. Diffraction indexing reveals a cubic structure, but not with a $\langle 111 \rangle$ growth direction of the columns, like in the three previous coatings. Indeed, the 111 spot position on the two diffraction patterns indicates that the $\{111\}$ planes are oriented parallel to the main axis of the columns. Indexing of the diffraction pattern shows that the growth direction of the column in Fig. 8a is $\langle 110 \rangle$, which has already been identified as a possible growth direction in SiC CVD coatings [18,45,46]. The growth direction of the column in Fig. 8b is less obvious. Based on the corresponding diffraction pattern (Fig. 8d), the (2,2,-4) diffracting planes, which are perpendicular to the (1,1,1) planes, are found perpendicular to the column axis (the 2,2,-4 spot is observed on the SAD pattern, but not shown in Fig. 8d because too far from the central spot). The growth direction of the column can then be defined as $\langle 112 \rangle$. This orientation has already been observed in the case of nanowire growth by catalyst-assisted vapor deposition [68] or CVD epitaxy on silicon substrate [69]. The diffraction pattern (Fig. 8d) also reveals the presence of a $\{111\}$ twin inside the column. The additional spots due to the twinned crystal are indexed “m” on the diffraction pattern. The twin plane splits the column in the height direction, as can be seen in the DF image (Fig. 8b). It should be noted that twins are considered included inside the columns for the column width measurements. The elongated 111 “m” spots in the diffraction pattern (Fig. 8d) suggest the presence of stacking faults within the column, perpendicular to its axis. The DF image (Fig. 8a,8b) of the interior of the columns is mottled (not striated as in the CR deposit columns) and not uniformly illuminated. This particular contrast might reveal the presence of structural defects inside the columns, for both $\langle 110 \rangle$ and $\langle 112 \rangle$ growth directions.

The microstructure of the MD coating (Fig. 9a), which is prepared at lower temperature than the regular MR coating, is significantly finer than that of MR. On the SAD pattern (Fig. 9b), a large number of spots are distributed over the Debye-Scherrer rings of the β structure, at 0.252 nm (111), 0.154 nm (220), and 0.131 nm (311). Such a pattern suggests that a large number of small crystals, without any marked preferential orientation, are included in the area selected for diffraction. The DF image (Fig. 9a) of the coating indeed reveals small elongated CDDs (<50 nm), relatively disoriented with respect to the growth axis of the coating. An example of these domains is shown in the HRTEM image (Fig. 9 c,d), where the 111 layers appear parallel to the axis of the columns, in a configuration similar to that of the CD2 coating. Thus, it appears that for both precursors, the decrease of the deposition temperature tends to favor growth along $\{111\}$ planes, as opposed to the flat stacking growth of the $\{111\}$ planes commonly observed for the other coatings.

3.4 Synthesis of the different analyses and discussion

The analyses conducted on the low temperature CVD coatings highlight their main common characteristic: they present a columnar morphology with a preferential orientation, typical of the growth mode of vapor deposited layers [70] and many structural defects, which are directly related to the low deposition temperature of the coatings. The objective is now to properly interpret the results of the different analyses, for the different materials, to correlate them to obtain an accurate description of the structure and microstructure of the deposits. For better readability, the main results associated with each coating and technique are gathered in [Table 4](#).

		RMS	HRTEM		XRD		
	Composition	« hexagonality » (%)	SFD (nm ⁻¹)	α phase ?	FWHM ₁₁₁ (°)	T ₁₁₁	T ₂₂₀
CR	SiC	40%	1.0	No	0.15	3.8	0
MR	SiC	7%	0.6	Yes	0.12	1.7	0.9
CD1	SiC + C sp²	33%	1.1	No	0.22	3.5	0
CD2	SiC	-	-	No	0.23	0.3	3
MD	SiC	-	-	No	0.81	1.3	1.2

[Table 4](#): Main characteristics of the SiC phase in the coatings

The purity of the SiC deposits (the absence of secondary phase such as free silicon or free carbon) SiC phase is easily revealed by Raman spectroscopy. All the coatings consist of pure SiC except CD1, which contains traces of disordered sp² carbon, as evidenced by the presence of broad D and G bands ([Fig. 2](#)). HRTEM analysis shows that this free carbon phase is localized at the interface between the columns, as a few isolated nanodomains ([Fig. 7c](#)). The distorted 002 fringes, separated by about 0.35 nm, are characteristic of pure turbostratic carbon, in agreement with the RMS analysis.

The texture of coatings, at the macroscopic scale, is easily accessible by XRD from the Harris coefficient ([Table 3](#)). The two specimens with the most pronounced <111> preferential orientation are CR and CD1. Consistently, in polarized RMS analysis, the spectra of the CR and CD1 samples are those for which the TO component varies most significantly with the polarization/orientation configuration ([Figs. 3a,3b](#)). The TEM local observations are also in good agreement with the Harris coefficient values: most of the columns have a <111> growth

direction (Figs. 5a,7b). The SAD diagram of the CD2 coating (Figures 8c,8d) shows that the columns appear to be predominantly oriented along the $\langle 110 \rangle$ direction, but also occasionally along the $\langle 112 \rangle$ direction. This coating indeed exhibits a T_{220} coefficient much higher than one ($T_{220} \approx 3$), the highest of all the coatings (Table 3). XRD analysis was extended beyond $2\theta = 90^\circ$ especially for this coating to evaluate the T_{224} coefficient. The value obtained ($T_{224} \approx 1.6$) confirmed that the $\langle 112 \rangle$ orientation is indeed present although not predominant. In the MD coating, on the other hand, the orientations along the $\langle 111 \rangle$, $\langle 110 \rangle$, and $\langle 311 \rangle$ directions are relatively balanced (Table 3). By TEM, the SAD pattern confirms the random orientation and the small size of the CDDs (Fig. 9b). A lattice fringe image (Fig. 9d) revealed an orientation of the $\{111\}$ planes parallel to the growth direction, consistent with a $\langle 110 \rangle$ or $\langle 112 \rangle$ preferential orientation of the grains. However, general conclusions about the texture of the coatings cannot be drawn from TEM analysis because of the very small scale considered by this technique compared to XRD.

The analysis of the disordered SiC phase in the material requires a more thorough combination of different techniques. The main origin of the disorder revealed by the diffraction techniques (XRD, TEM) is obviously the repetition of the stacking defects of the Si-C bilayers in the CDDs, whatever their arrangement within the columns. SFs result from a 1D sequence of $\Sigma 3$ microtwins along $\{111\}$ planes, in a particular direction of a CDD. If these fault are frequently and randomly distributed in the stacking, a specific ODD polytype is defined, which differs from the β and any of the α polytypes in that it does not present periodicity in the stacking direction [28]. TEM analysis is well suited to identify this polytype, from the characteristic SAD pattern (showing lateral straight lines parallel to the $\langle 111 \rangle$ direction, Fig. 5a) or HRTEM image (with random contrast lines, Fig. 6a) of a single CDD. Based on this criterion, the CR coating seems to be the most representative of an ODD polytype. The density of stacking faults (SFD), as measured by HRTEM, is an another important parameter to rule on the existence and better define an ODD polytype. A remarkable correlation can be found, for the different deposits, between the SFD value deduced from the TEM contrast lines and the ΔTO peak splitting measured from the Raman spectra. Indeed, the SFD / TO values are very close in the case of CR and CD1, while those of MR are clearly different (Table 4). These results are consistent because ΔTO , like the SFD value, reflects the percentage of hexagonal layers in the polytype stacking sequence, either in periodic [19,52] or ODD [2,61] polytypes. The SFD and TO values deduced by HRTEM and RMS are both relative to the entire 1D faulted crystalline domains, i.e. to CDDs. According to Pujar and Cawley, more precise information can be

inferred from XRD analyses by subdividing CDDs into two distinct fault-free and faulted – Ising – domains (FFDs and IDs) [40-42]. This approach suggests that, in the MR coating, the CDDs contain rather large FFDs (consistent with the low $FWHM_{111}$ value), including a high density of intrinsic SFs, in agreement with the d_{SF} value of 0.266 nm (Fig. 1). Such a high density of SFs can become periodical and generate small α domains (Figs. 5b,6b), which is not incompatible with an ODD structure according Shinozaki [28]. In comparison, in the CR coating, the distribution of SFs would be more homogeneous in the CDDs, leading to a more interlocking distribution of FDDs and IDs, preventing the occurrence of periodic sequences. CD1 would be relatively similar to CR in terms of relative ID/FFD size and SF density, but would contain smaller coherent domains, explaining the higher $FWHM_{111}$ value (Table 4). This description remains consistent with the overall hexagonal character of the three coatings: the difference in the relative ID/FDD size compensating for that of the SF density in the IDs.

Another type of disorder, more substantial than that inherent to stacking faults, is highlighted by RMS analysis. It is particularly pronounced in the CD2 and MD coatings (Fig. 2). In MD, these high energy structural defects seem clearly related to the fine microstructure of the material. The $FWHM_{111}$ is indeed particularly high for this coating (Table 4), reflecting a particularly small average CDD size (Fig 1). The structural units are indeed much smaller (< 50 nm) than in the other coatings (Fig 9a), so the grain boundaries, which are sites of strong structural disorders, are particularly abundant. In the CD2 coating, which is also severely disordered according to RMS, the origin of disorder is more difficult to determine. From TEM analysis, the microstructure is columnar, with diffracting columns several hundred nanometers wide. However, numerous crystalline defects are revealed within these domains by TEM-DF images (Figs. 8a,8b). In these <110> or <112> oriented columns, the {111} planes are parallel to the column axis (and the growth direction). In such a configuration of the {111} planes in the coating, Nishiguchi *et al.* highlighted the presence of many structural defects related to cancellations or changes in the mean orientation of the stacking faults [69]. Sundaresan *et al.* also illustrated how the <112> oriented growth of SiC nanowires can generate frequent microtwins disrupting the structural ordering [68]. Examples of structural defects identified in CD2 coating are presented in Fig. 10. By magnifying an area with stacking faults parallel to the growth direction (Fig. 10b), the SF cancellations are highlighted by the interruption the contrast lines (or bands), indicated by white arrows [69]. In another area of the coating, with a mottled contrasting aspect, the inverse fast Fourier transform (IFFT) of a detail of the HRTEM image (Fig. 10d) was used to reveal the high density of dislocations (marked with a white T-mark).

Such dislocations have also been revealed by IFFT analysis in disturbed transition areas between 6H and 3C forms of SiC [39]. Recently, Zimbone *et al.* have better described combinations between SFs and dislocations in epitaxial 3C SiC by high-angle annular dark-field scanning transmission electron microscopy (HAADF-STEM), with Si-C dimer displaying [71]. These authors found that the stacking defects are bordered by two partial dislocations that limit the wrong sequence plane from the perfect 3C regions and that the "boundaries" along the {111} planes are composed of Si-Si bonds. The CD2 defects, which are particularly abundant, introduce large components on the Raman spectrum and, in addition, alter the diffraction contrast of TEM-DF images. They do not broaden $FWHM_{111}$ as significantly as in MD but seem to generate a large amount of intrinsic SFs, as shown by the presence of a fine peak at 0.266 nm (Fig. 1). This type of disorder has been identified in $\langle 110 \rangle$ and $\langle 112 \rangle$ oriented columns (in CD2), but not in $\langle 111 \rangle$ oriented columns (in both CR and MR). The crystal growth mechanism is of course different whether it occurs along the $\langle 110 \rangle$, $\langle 112 \rangle$ or $\langle 111 \rangle$ direction. It appears that many more crystal defects are created in the first two cases, when the stacks of {111} planes grow laterally, parallel to the coating growth direction – as opposed to the classical growth by flat stacking, layer by layer, of {111} planes. In other words, "pure ODD" domains tend to extend across the entire width of the "columnar unit" in the case of $\langle 111 \rangle$ preferential orientation, whereas they are reduced to nanodomains in the columns oriented along the $\langle 110 \rangle$ and $\langle 112 \rangle$ directions.

Finally, the nature of the various CVD SiC deposits can be tentatively correlated with their processing conditions. At relatively high temperature ($T > 1000^\circ\text{C}$), when the deposition rate tends to be limited by mass transfer [8], the surface diffusion is fast so that reactive species and adatoms can reach stable growth sites forming a well-crystallized deposit. In these conditions, using a conventional $\text{CH}_3\text{SiCl}_3/\text{H}_2$ mixture, the β -SiC coating often exhibits a $\langle 111 \rangle$ fiber texture resulting from a growth by successive stacking of Si and C atomic layers, parallel to the substrate [9,12,13]. This process is accompanied by stacking faults in the 3C structure, forming the ODD polytype mentioned above, which involves only low energy defects. The structure and microstructure of the CR coating is well representative of this type of deposit. From a chemical point a view, the unimolecular decomposition of CH_3SiCl_3 leads to SiCl_3 and CH_3 radicals, from low temperatures and residence times [72-75]. At higher T and τ_r values, other species like SiCl_2 appear in the gas phase, which also contribute to the coating. SiCl_3 , SiCl_2 and CH_3 are chemisorbed on the {111} planes of the growing SiC substrate [74]. Similarly, for the $\text{SiHCl}_3/\text{C}_3\text{H}_8$ system, SiCl_3 and SiCl_2 are produced by decomposition of SiHCl_3 [36]. Although

the hydrocarbons derived from C_3H_8 are more abundant and diverse than from CH_3SiCl_3 , CH_3 remains one of the main effective carbon precursors (with other C_2 radicals). C_2H_2 may also appear, contributing to the deposition of free carbon at particularly high T , τ , or C_3H_8 ratios [36]. The typical columnar microstructure and the ODD polytype structure observed for the CR coating are probably related to the similar chemistry of both CH_3SiCl_3 and $SiHCl_3/C_3H_8$ systems. The CD1 coating is obtained with the same precursors and temperature, but with a different gas composition (Table 1). Although the changes in the $H_2/HSiCl_3$ and $C_3H_8/HSiCl_3$ gas ratios tend to balance out the Si/C ratio in the solid, this deposit contains a slight excess of carbon, which is probably related to the formation of C_2H_2 in the gas phase [36]. The co-deposited carbon nanodomains inhibit the crystal growth, resulting in thinner and more disoriented SiC columns with a slightly higher density of stacking faults. The MR coating is processed with a radically different precursor (CH_3SiH_3). This precursor is significantly less stable than chloro(carbo)silanes [76-78], allowing SiC deposition at much lower temperature, pressure and concentration [37,79-82]. In this case, CH_3SiH_3 is probably directly chemisorbed on the surface to form SiC [37]. Coatings are usually polycrystalline at 900°C or higher [79,80], but also at lower temperatures [82], and they can even be sometimes monocrystalline (3C) [83]. This ability to form crystalline SiC from low temperatures can be found for the MR deposit. Despite the low deposition temperature, this coating is relatively well crystallized: the columns are slightly less wide than in CR but have a significantly lower density of stacking faults. Such a decrease in stacking fault density with decreasing temperature was simulated by DFT calculations [84]. The decrease of the deposition temperature results, for both precursor systems, in a much less crystalline coating: CD2 and MD (by limiting the formation of reactive unsaturated hydrocarbons, it also avoids the co-deposition of free carbon). It also causes the texture to change to $\langle 110 \rangle$. A 2D nucleation model relating preferential orientation, supersaturation and surface energy was developed by Pangarov [85,86] and refined by Lee [15]. These authors showed that these conditions of higher gas phase supersaturation and slower surface diffusion can lead to a transition in preferential orientation in the coating, from planes with the lowest surface energy to those with the highest surface energy. In the case of β -SiC, this phenomenon could explain the texture transition from $\langle 111 \rangle$ to $\langle 110 \rangle$ at lower temperature. For the same reasons (high supersaturation, slow diffusion), such a texture transition is associated with a greater number of interruptions in crystal growth, which cause more energetic structural defects than stacking faults. These defects are concentrated at the boundaries of the ODD domains, either at the interface between the small columns of the MD coating, or within the larger columns of CD2.

4 Conclusion

This study focuses on little explored materials although of great societal relevance: low temperature CVD SiC coatings for ceramic matrix composites and thermo-structural applications. It demonstrates how peculiar – and defective – the structure of these materials is compared to those of sintered or epitaxial SiC, which have been much more widely studied.

TEM, XRD and RS are three complementary techniques adapted to structural and microstructural analysis, as they characterize different scales of the material. Each of them is sensitive to specific characteristics of the material (chemical composition, structural order and disorder, texture). Their combination allowed a comparative analysis of various CVD coatings (Table 4) prepared at low temperature, under distinct and well-controlled conditions. The coatings are polycrystalline, of 3C cubic structure and present a columnar microstructure associated with a preferential orientation, and a variety of structural disorders. The different coatings can be differentiated on the basis of the nature and proportion of these structural defects. When the {111} planes grow perpendicular to the growth direction (according to a $\langle 111 \rangle$ texture), the periodicity in the stacking direction of the Si-C bilayers is almost always interrupted, generating numerous and randomly distributed stacking faults (with a density of at least 1 nm^{-1}). This gives rise to the well-known one-dimensionally-disordered (ODD) polytype. This structure/microstructure is typically obtained at relatively high temperature (within a mass transfer-controlled regime) from CH_3SiCl_3 or $\text{SiHCl}_3/\text{C}_3\text{H}_8$, probably via the same effective precursors (SiCl_3 , SiCl_2 , CH_3). The frequency and spatial distribution of stacking faults can vary within coherent domains, and locally generate periodic sequences, identified as α polytypes. Methylsilane seems to be more suitable to obtain this type of structure. The direct adsorption of CH_3SiH_3 on the growing surface could explain its ability to form crystalline SiC at a relatively low temperature, compared to more conventional chlorinated precursors.

Disorder in the coatings is localized in the random stacking of Si-C bilayers and at the column boundaries, as higher energy defects, which are more abundant as the columns are smaller. When the coatings grow with the {111} planes parallel to the growth direction (via a $\langle 110 \rangle$ or $\langle 112 \rangle$ texture), a specific type of disorder, also more energetic than stacking faults, is introduced within the columns themselves. The ODD domains are frequently interrupted and the boundaries between them, which are now parallel to the growth axis, are the seat of crystal distortions, involving for example dislocations.

An accurate and combined exploitation of the TEM and Raman results allows to distinguish and clearly describe defects among the various structural imperfections of CVD coatings deposited at low temperature. The contribution of TEM is essential as it has the great advantage of directly imaging the microstructure. But it can be limited in the case of disordered materials like those studied here. On the other hand, the disadvantage of Raman spectroscopy is the difficulty to categorize defects simply from the spectral features. The complementary contribution of both TEM and Raman analysis is therefore essential. A modeling of the spectra based on structural atomistic models representative of the TEM observations would be very attractive, but this approach is particularly complex in the case of resonant phenomena like those encountered here. This detailed analysis various low temperature CVD SiC coatings shows that it is possible to adjust the (micro)structure by selecting the precursor molecules and adjusting the CVD conditions (*e.g.* the temperature, initial gas composition, supersaturation...). The effects of these parameters are relatively simple to explain, at least qualitatively. A more quantitative description of the relationship between the CVD conditions and the (micro)structure is much more difficult. Firstly, because the homogeneous mechanisms associated with the chemical systems investigated here are still questionable and secondly, because the heterogeneous mechanisms must take into account the presence of various and numerous defects, present on the substrate surface and continuously incorporated in the growing solid.

Acknowledgements

The authors acknowledge Safran Ceramics, the National Center for Scientific Research (CNRS), and the French National Association for Research and Technology (ANRT) for their help and financial support to I.B. (CIFRE contract N°2015/1352), G.L. (CNRS contract N°084063) and A.D (CIFRE contract N° 2015/1426). H.P. especially thanks Eric Bouillon, scientific director of Safran Ceramics, for encouraging him to conduct academic research on the microstructure of ceramic composites.

References

[1] L. L. Snead, T. Nozawa, Y. Katoh, T.-S. Byun, S. Kondo, D. A. Petti, Handbook of SiC properties for fuel performance modeling, J. Nucl. Mater. 371 (2007) 329–377.

- [2] R. A. Shatwell, K. L. Dyos, C. Prentice, Y. Ward, R. J. Young, Microstructural analysis of silicon carbide monofilaments, *J. Microsc.* 201(2) (2001) 179–188. <https://doi.org/10.1046/j.1365-2818.2001.00836.x>
- [3] P. R. Smith, M. L. Gambone, D. S. Williams, D. I. Garner, Heat treatment effects on SiC fiber, *J. Mater. Sci.* 33 (1998) 5855–5872. <https://doi.org/10.1023/A:1004478804694>
- [4] J. A. DiCarlo, H. M. Yun, Factors controlling stress-rupture of fiber-reinforced ceramic matrix composites, Proceedings of the 1999 International Conference on Composite Materials, A. Vautrin, T. Massard eds., CD-ROM, 1999. <https://www.iccm-central.org/Proceedings/ICCM12proceedings/site/papers/pap750.pdf>
- [5] G. Chollon, R. Naslain, C. Prentice, R. A. Shatwell, P. May, High temperature properties of SiC and diamond CVD-monofilaments, *J. Eur. Ceram. Soc.* 25 (2005) 1929–1942. <https://doi.org/10.1016/j.jeurceramsoc.2004.06.013>
- [6] R. Naslain, SiC-Matrix Composites: Nonbrittle Ceramics for Thermo-Structural Application *Int. J. App. Ceram. Technol.* 2 (2005) 5-84. <https://doi.org/10.1111/j.1744-7402.2005.02009.x>
- [7]: R. Naslain, F. Langlais, R. Fedou, The CVI processing of ceramic matrix composites *J. Phys. Colloq.* 50(C5) (1989) 191–207. <https://doi.org/10.1051/jphyscol:1989526>
- [8] F. Loumagne, F. Langlais, R. Naslain, Experimental kinetic study of the chemical vapour deposition of SiC-based ceramics from $\text{CH}_3\text{SiCl}_3/\text{H}_2$ gas precursor, *J. Cryst. Growth* 155 (1995) 198–204. [https://doi.org/10.1016/0022-0248\(95\)00180-8](https://doi.org/10.1016/0022-0248(95)00180-8)
- [9] F. Loumagne, F. Langlais, R. Naslain, S. Schamm, D. Dorignac, J. Sévely, Physicochemical properties of SiC-based ceramics deposited by low pressure chemical vapor deposition from $\text{CH}_3\text{SiCl}_3\text{-H}_2$, *Thin Solid Films* 254 (1995) 75–82. [https://doi.org/10.1016/0040-6090\(94\)06237-F](https://doi.org/10.1016/0040-6090(94)06237-F)
- [10] T. D. Gulden, Deposition and microstructure of vapor-deposited silicon carbide, *J. Am. Ceram. Soc.*, 51 (1968) 424–427. <https://doi.org/10.1111/J.1151-2916.1968.TB11911.X>
- [11] D. Lespiaux, F. Langlais, R. Naslain, S. Schamm, J. Sevely, Correlations between gas phase supersaturation nucleation process and physico-chemical characteristics of silicon carbide deposited from Si-C-H-Cl system on silica substrates, *J. Mater. Sci.* 30 (1995) 1500–1510. <https://doi.org/10.1007/BF00375255>

- [12] S. Schamm, A. Mazel, D. Dorignac, J. Sévely, HREM identification of “one-dimensionally-disordered” polytypes in the SiC (CVI) matrix of SiC/SiC composites, *Microsc. Microanal. Microstruct.* 2 (1991) 59–73. <https://doi.org/10.1051/mmm:019910020105900>
- [13] D.P. Stinton, D.M. Hembree, K.L. More, B.W. Sheldon, T.M. Besmann, M.H. Headinger, R.F. Davis, Matrix characterization of fibre-reinforced SiC matrix composites fabricated by chemical vapour infiltration, *J. Mater. Sci.* 30 (1995) 4279–4285. <https://doi.org/10.1007/BF00361507>
- [14] J. Chin, P. K. Gantzel R.G. Hudson, The structure of chemical vapor deposited silicon carbide, *Thin Solid Films* 40 (1977) 57–72. [https://doi.org/10.1016/0040-6090\(77\)90103-1](https://doi.org/10.1016/0040-6090(77)90103-1)
- [15] D. Lee, “A model for development of orientation of vapour deposits”, *J. Mater. Sci.* 24 1989 4375–4378. <https://doi.org/10.1007/BF00544515>
- [16] B.J. Choi, S.H. Jeun, D.R. Kim, The effects of C₃H₈ on the chemical vapor deposition of silicon carbide in the CH₃SiCl₃ + H₂ system, *J. Eur. Ceram. Soc.* 9 (1992) 357–363. [https://doi.org/10.1016/0955-2219\(92\)90094-T](https://doi.org/10.1016/0955-2219(92)90094-T)
- [17] D. Kuo, D. Cheng, W. Shyy, M. Hon, “Effect of CH₄ on CVD β-SiC growth”, *J. Electrochem. Soc.* 137 (1990) 3688–3692. <https://doi.org/10.1149/1.2086288>
- [18] S. Zhang, Q. Xu, R. Tu, T. Goto, L. Zhang, “High-speed preparation of <111>- and <110>-oriented β-SiC films by laser chemical vapor deposition”, *J. Am. Ceram. Soc.*, 97 (2014) 952–958. <https://doi.org/10.1111/jace.12706>
- [19] D. W. Feldman, J. H. Parker Jr, W. J. Choyke, L. Patrick, Phonon Dispersion Curves by Raman Scattering in SiC Polytypes 3C, 4H, 6H, 15R and 21R, *Phys. Rev.* 173 (1968) 787–793. <https://doi.org/10.1103/PhysRev.173.787>
- [20] S. Nakashima, H. Katahama, Y. Nakakura, A. Mitsuishi, Relative Raman intensities of the folded modes in SiC polytypes, *Phys. Rev.* B33 (1986) 5721–5729. <https://doi.org/10.1103/physrevb.33.5721>
- [21] R. Loudon, The Raman effect in crystals, *Adv. Phys.* 52 (1964) 423–482. <https://doi.org/10.1080/00018736400101051>
- [22] Y. Sasaki, Y. Nishina, M. Sato, K. Okamura, “Raman study of SiC fibres made from polycarbosilane”, *J. Mater. Sci.* 22 (1987) 443–448. <https://doi.org/10.1007/BF01160751>

- [23] Y. Ward, R. J. Young, R. A. Shatwell, Microstructural study of silicon carbide fibers through the use of Raman microscopy, *J. Mater. Sci.* 36 (2001) 55–66. <https://doi.org/10.1023/A:1004830505979>
- [24] S.-L. Zhang, B.-F. Zhu, F. Huang, Y. Yan, E.-Y. Shang, S. Fan, W. Han, Effect of defects on optical phonon Raman spectra in SiC nanorods, *Solid State Commun.* 111 (1999) 647–651. [https://doi.org/10.1016/S0038-1098\(99\)00262-8](https://doi.org/10.1016/S0038-1098(99)00262-8)
- [25] Y. Yan, S.-L. Zhang, S. Fan, W. Han, G. Meng, L. Zhang, Effect of changing incident wavelength on Raman features of optical phonons in SiC nanorods and TaC nanowires, *Solid State Commun.* 126, (2003) 649–651 [https://doi.org/10.1016/S0038-1098\(03\)00236-9](https://doi.org/10.1016/S0038-1098(03)00236-9)
- [26] Y. Ward, R. J. Young, R. A. Shatwell, Effect of excitation wavelength on the Raman scattering from optical phonons in silicon carbide monofilaments, *J. Appl. Phys.* 102 (2007) 023512. <https://doi.org/10.1063/1.2751412>
- [27] Z. Xiao, Y. Yang, S. Ouyang, Z. Kou, B. Huang, X. Luo, Raman investigation of defective SiC nanocrystals, *J. Raman Spectrosc.* 46 (2015) 1225–1229. <https://doi.org/10.1002/jrs.4769>
- [28] S. Shinozaki, K.R. Kinsman, Aspects of "one dimensional disorder" in silicon carbide, *Acta Metallurgica*, 26 (1978) 769-776. [https://doi.org/10.1016/0001-6160\(78\)90027-5](https://doi.org/10.1016/0001-6160(78)90027-5)
- [29] N.W. Jepps, D.J. Smith, T.F. Page, The direct identification of stacking sequences in silicon carbide polytypes by high-resolution electron microscopy, *Acta Crystall. Sect. A*, 35 (1979) 916–923. <https://doi.org/10.1107/S0567739479002059>
- [30] S. Klein, L. Houben, R. Carius, F. Finger, W. Fischer, Structural properties of microcrystalline SiC deposited at low substrate temperatures by HWCVD, *J. Non-Crystal. Solids* 352 (2006) 1376–1379 <https://doi.org/10.1016/j.jnoncrysol.2006.01.047>
- [31] M. Havel D. Baron L. Mazerolles P. Colomban, Phonon Confinement in SiC Nanocrystals: Comparison of the Size Determination Using Transmission Electron Microscopy and Raman Spectroscopy, *Appl. Spectrosc.* 61 (2007) 855–859. <https://doi.org/10.1366/000370207781540187>
- [32] E. López-Honorato, P.J. Meadows, J. Tan, Y. Xiang, P. Xiao, Control of stoichiometry, microstructure, and mechanical properties in SiC coatings produced by fluidized bed chemical vapor deposition, *J. Mater. Res.* 23 (2008) 1785–1796. <https://doi.org/10.1557/JMR.2008.0220>

- [33] Carduner, K.R., Shinozaki, S.S., Rokosz, M.J., Peters, C.R., Whalen, T.J. Characterization of β -Silicon Carbide by Silicon-29 Solid-State NMR, Transmission Electron Microscopy, and Powder X-ray Diffraction (1990) *Journal of the American Ceramic Society*, 73 (8), pp. 2281–2286. <https://doi.org/10.1111/j.1151-2916.1990.tb07589.x>
- [34] E. López-Honorato, C. Brigden, R.A. Shatwell, H. Zhang, I. Farnan, P. Xiao, P. Guillermier, J. Somers, Silicon carbide polytype characterisation in coated fuel particles by Raman spectroscopy and ^{29}Si magic angle spinning NMR, *J. Nucl. Mater.* 433 (2013) 199–205. <https://doi.org/10.1016/j.jnucmat.2012.08.047>
- [35] T. D. Gulden, Stacking Faults in Chemically-Vapor-Deposited Beta Silicon Carbide, *J. Am. Ceram. Soc.* 54 (1971) 498–501. <https://doi.org/10.1111/j.1151-2916.1971.tb12187.x>
- [36] G. Laduye, CVD du carbure de silicium à partir du système $\text{SiH}_x\text{Cl}_{4-x}/\text{C}_y\text{H}_z/\text{H}_2$: étude expérimentale et modélisation, PhD Thesis, University of Bordeaux, 2016. <https://tel.archives-ouvertes.fr/tel-01477657>
- [37] A. Desenfant, Dépôt par voie gazeuse de carbure de silicium à partir de précurseurs alternatifs au methyltrichlorosilane, Ph-D Thesis, University of Bordeaux, 2018. <http://www.theses.fr/2018BORD0353>
- [38] A. Desenfant, G. Laduye, G. Vignoles, G. Chollon, Kinetic and gas-phase study of the chemical vapor deposition of silicon carbide from $\text{C}_2\text{H}_5\text{SiCl}_3/\text{H}_2$, *J. Industr. Engin. Chem.* 94 (2021) 145–158. <https://doi.org/10.1016/j.jiec.2020.10.029>
- [39] R. Vasiliasuskas, M. Marinova, M. Syväjärvi, E.K. Polychroniadis, R. Yakimova, Polytype transformation and structural characteristics of 3C-SiC on 6H-SiC substrates, *J. Cryst. Growth* 395 (2014) 109–115. <https://doi.org/10.1016/j.jcrysgro.2014.03.021>
- [40] V.V. Pujar, J.D. Cawley, Effect of Stacking Faults on the X-ray Diffraction Profiles of β -SiC Powders, *J. Am. Ceram. Soc.* 78 (1995) 774–782. <https://doi.org/10.1111/j.1151-2916.1995.tb08246.x>
- [41] V.V. Pujar, J.D. Cawley, Computer simulations of diffraction effects due to stacking faults in β -SiC: I, simulation results, *J. Am. Ceram. Soc.* 80 (1997) 1653–1662. <https://doi.org/10.1111/j.1151-2916.1997.tb03034.x>
- [42] V.V. Pujar, J.D. Cawley, Computer Simulations of Diffraction Effects due to Stacking Faults in β -SiC: II, Experimental Verification, *J. Am. Ceram. Soc.*, 84 (2001) 2645–2651 <https://doi.org/10.1111/j.1151-2916.2001.tb01066.x>

- [43] D. Gosset, C. Colin, A. Jankowiak, T. Vandenberghe, N. Lochet, X-ray Diffraction Study of the Effect of High-Temperature Heat Treatment on the Microstructural Stability of Third-Generation SiC Fibers, *J. Am. Ceram. Soc.* 96 (2013) 1622–1628. <https://doi.org/10.1111/jace.12174>
- [44] D.J. Sprouster, T. Koyanagi, E. Dooryhee, S.K. Ghose, Y. Katoh, L.E. Ecker, Microstructural evolution of neutron irradiated 3C-SiC, *Scripta Mater.* 143 (2018) 176–180. <https://doi.org/10.1016/j.scriptamat.2017.09.034>
- [45] So, M.G., Chun, J.S. Growth and structure of chemical vapor deposited silicon carbide from methyltrichlorosilane and hydrogen in the temperature range of 1100 to 1400°C, *J. Vac. Sci. Techn. A* 6(1988) 5–8. <https://doi.org/10.1116/1.574969>
- [46] H. Cheng, R. Tu, S. Zhang, M. Han, T.Goto, L. Zhang, Preparation of highly oriented β -SiC bulks by halide laser chemical vapor deposition, *J. Eur. Ceram. Soc.* 37 (2017) 509-515. <https://doi.org/10.1016/j.jeurceramsoc.2016.09.017>
- [47] Lai, Y., Zhao, S., Luo, T., Xu, Q., Liu, C., Liu, K., Li, Q., Yang, M., Zhang, S., Han, M., Goto, T., Tu, R. Microstructure and texture of polycrystalline 3C-SiC thick films characterized via EBSD (2020) *Ceramics International*, 46 (17), pp. 27000-27009. <https://doi.org/10.1016/j.ceramint.2020.07.177>
- [48] G.B. Harris, Quantitative measurement of preferred orientation in rolled uranium bars, *Philos. Mag. Ser.*, 7(1952) 113–123. <https://doi.org/10.1080/14786440108520972>
- [49] V. Valvoda, M. Järvinen, On The Harris Texture Index. *Powder Diffraction*, 5(1990) 200-203. <https://doi.org/10.1017/S0885715600015797>
- [50] G.K Williamson, W.H Hall, X-ray line broadening from filed aluminum and wolfram, *Acta Metallurgica* 1 (1953) 22–31. [https://doi.org/10.1016/0001-6160\(53\)90006-6](https://doi.org/10.1016/0001-6160(53)90006-6)
- [51] J. Yeomans, The Theory and Application of Axial Ising Models, *Solid State Phys. – Adv. Res. Appl.* 41 (1988) 151–200. [https://doi.org/10.1016/S0081-1947\(08\)60379-3](https://doi.org/10.1016/S0081-1947(08)60379-3)
- [52] D. W. Feldman, J. H. Parker Jr, W. J. Choyke, L. Patrick, Raman scattering in 6H SiC, *Phys. Rev.* 170 (1968) 787–793. <https://doi.org/10.1103/PhysRev.170.698>
- [53] G. Chollon, Structural and textural analyses of SiC-based and carbon CVD, *Thin Solid Films*, 516 (2007) 388–396. <https://doi.org/10.1016/j.tsf.2007.06.098>
- [54] F. Tuinstra, J. L. Koenig, Raman Spectrum of Graphite, *J. Chem. Phys.* 33 (1970) 1126–1130. <https://doi.org/10.1063/1.1674108>

- [55] A. Cuesta, P. Dahmelincourt, J. Laureyns, A. Martinez-Alonzo, J.M.D. Tarascon, Raman microprobe study on carbon materials, *Carbon*, 32 (1994) 1523–1532. [https://doi.org/10.1016/0008-6223\(94\)90148-1](https://doi.org/10.1016/0008-6223(94)90148-1)
- [56] H. Richter, Z. P. Wang, L. Ley, The one phonon Raman spectrum in microcrystalline silicon, *Solid State Commun.* 39 (1981) 625–629. [https://doi.org/10.1016/0038-1098\(81\)90337-9](https://doi.org/10.1016/0038-1098(81)90337-9)
- [57] I.H. Campbell, P.M. Fauchet, The effects of microcrystal size and shape on the one phonon Raman spectra of crystalline semiconductors, *Solid State Commun.* 58 (1986) 739–741. [https://doi.org/10.1016/0038-1098\(86\)90513-2](https://doi.org/10.1016/0038-1098(86)90513-2)
- [58] S. Nakashima, H. Ohta, M. Hangyo, B. Palosz, Phonon Raman scattering in disordered silicon carbides, *Philos. Mag. B* 70 (1994) 971–985. <https://doi.org/10.1080/01418639408240266>
- [59] S. Rohmfeld, M. Hundhausen, L. Ley, F. Tuinstra, J. L. Koenig, Influence of Stacking Disorder on the Raman Spectrum, *Phys. Stat. Sol.* 215 (1999) 115–119. [https://doi.org/10.1002/\(SICI\)1521-3951\(199909\)215:1<115::AID-PSSB115>3.0.CO;2-3](https://doi.org/10.1002/(SICI)1521-3951(199909)215:1<115::AID-PSSB115>3.0.CO;2-3)
- [60] G. Chollon, Structural and textural changes of CVD-SiC to indentation, high temperature creep and irradiation, *J. Eur. Ceram. Soc.* 27 (2007) 1503–1511. <http://dx.doi.org/10.1016/j.jeurceramsoc.2006.05.038>
- [61] Y. Ward, R. J. Young, R. A. Shatwell, Application of Raman microscopy to the analysis of silicon carbide monofilaments, *J. Mater. Sci.* 39 (2004) 6781–6790. <https://doi.org/10.1023/B:JMSE.0000045606.60263.27>
- [62] G. Chollon, J.M. Vallerot, K. Grente, R. A. Shatwell, M. Couzi, Local texture analyses of ceramic and carbon composites through Raman micro-spectroscopy mappings, in: *High temperature ceramic matrix composites 5: proceedings of the 5th International Conference on High Temperature Ceramic Matrix Composites (HTCMC 5)*, M. Singh, R.J. Kerans, E. Lara-Cursio, R. Naslain eds., the American Ceramic Society, Westerville, Ohio, 2005, pp. 557–562.
- [63] S.-L. Zhang, Y. Zhang, W. Liu, Z. Fu, Y. Yan, J. Chen, R. Ma, Y. Song, J. Zhao, L.-S. Xu, S. Wu, M. Gao, H. Li, Lack of dependence of the Raman frequency of optical vibrational modes on excitation wavelength in polar nanosemiconductors, *Appl. Phys. Lett.* 89 (2006) 063112. <https://doi.org/10.1063/1.2335622>

[64] B. Reznik, D. Gerthsen, W. Zhang, K.J. Hüttinger, Microstructure of SiC deposited from methyltrichlorosilane, *J. Eur. Ceram. Soc.* 23 (2003) 1499–1508.

[http://dx.doi.org/10.1016/S0955-2219\(02\)00364-3](http://dx.doi.org/10.1016/S0955-2219(02)00364-3)

[65] S. S. Shinozaki, H. Sato, Microstructure of SiC Prepared by Chemical Vapor Deposition, *J. Am. Ceram. Soc.* 61 (1978) 425–429. <https://doi.org/10.1111/j.1151-2916.1978.tb09352.x>

[66] B. Chayasombat, Y. Kimata, T. Tokunaga, K. Kuroda, K. Sasaki, Microstructure characterization of defects in cubic silicon carbide using transmission electron microscopy, *Microscopy Microanal.* 19 [Suppl. 5] (2013) 119–122. <https://doi.org/10.1017/S1431927613012464>

[67] T. Uchimaru, N. Ohmori, Y. Abe, J. Komiyama, Evaluation of stacking faults in single-crystalline 3C-SiC films by polarized Raman spectroscopy, *Japan. J. Appl. Phys.* 52 (2013) N° 075501 <https://doi.org/10.7567/JJAP.52.075501>

[68] Sundaresan, S.G., Davydov, A.V., Vaudin, M.D., Levin, I., Maslar, J.E., Tian, Y.-L., Rao, M.V. Growth of silicon carbide nanowires by a microwave heating-assisted physical vapor transport process using group VIII metal catalysts (2007) *Chemistry of Materials*, 19 (23), pp. 5531-5537. <https://doi.org/10.1021/cm071213r>

[69] T. Nishiguchi, Y. Mukai, M. Nakamura, K. Nishio, T. Isshiki, S. Ohshima, S. Nishino, Structural analysis of (211) 3C-SiC on (211) Si substrates grown by chemical vapor deposition *Materials Science Forum*, 457-460 (2004) 285-288. <https://doi.org/10.4028/www.scientific.net/msf.457-460.285>

[70] Van der Drift A., Evolutionary selection, a principle governing growth orientation in vapour-deposited layers. *Philips Res Rep* 22(1967)267-288.

[71] Zimbone, M., Sarikov, A., Bongiorno, C., Marzegalli, A., Scuderi, V., Calabretta, C., Miglio, L., La Via, F. Extended defects in 3C-SiC: Stacking faults, threading partial dislocations, and inverted domain boundaries (2021) *Acta Materialia*, 213, art. no. 116915. <https://doi.org/10.1016/j.actamat.2021.116915>

[72] S.-I. Motoyama, N. Morikawa, S. Kaneda, “Low-temperature growth and its growth mechanisms of 3C-SiC crystal by gas source molecular beam epitaxial method”, *J. Cryst. Growth* 100 (1990) 615–626. [https://doi.org/10.1016/0022-0248\(90\)90260-R](https://doi.org/10.1016/0022-0248(90)90260-R)

[73] G. D. Papasouliotis, S. V. Sotirchos, “On the Homogeneous Chemistry of the Thermal Decomposition of Methyltrichlorosilane: Thermodynamic Analysis and Kinetic Modeling”, *J.*

Electrochem. Soc. 141 (1994) 1599–1611. <https://doi.org/10.1149/1.2054969>

[74] F. Loumagne, F. Langlais, R. Naslain, Reactional mechanisms of the chemical vapour deposition of SiC-based ceramics from $\text{CH}_3\text{SiCl}_3/\text{H}_2$ gas precursor, J. Cryst. Growth 155 (1995) 205–213. [https://doi.org/10.1016/0022-0248\(95\)00181-6](https://doi.org/10.1016/0022-0248(95)00181-6)

[75] M. Ganz, N. Dorval, M. Lefebvre, M. Péalat, F. Loumagne, F. Langlais, “In situ optical analysis of the gas phase during the deposition of silicon carbide from methyltrichlorosilane”, J. Electrochem. Soc. 143 (1996) 1654–1661. <https://doi.org/10.1149/1.1836694>

[76] I. M. Davidson, M. A. Ring, “Primary processes in the low-pressure pyrolysis of methylsilane”, J. Chem. Soc. Faraday Trans. 76 (1980) 1520–1525.

<https://doi.org/10.1039/F19807601520>

[77] B.A. Sawrey, H.E. O’Neal, M.A. Ring, D. Coffey JR., The gas-phase decomposition of methylsilane. Part III. Kinetics, Int. J. Chem. Kinetics 16 (1984) 31–39. <https://doi.org/10.1002/kin.550160106>

[78] M.S. Gordon, T.N. Truong, Potential primary pyrolysis processes of methylsilane, Chem. Phys. Lett. 142 (1987) 110–114. [https://doi.org/10.1016/0009-2614\(87\)87261-5](https://doi.org/10.1016/0009-2614(87)87261-5)

[79] A.D. Johnson, J. Perrin, J.A. Mucha, D.E. Ibbotson, Kinetics of silicon carbide CVD: surface decomposition of silacyclobutane and methylsilane, J. Phys. Chem. 97 (1993) 12937–12948. <https://doi.org/10.1021/j100151a049>

[80] A.M. Abyzov, E.P. Smirnov, Kinetics of SiC chemical vapor deposition from methylsilane, Inorganic Materials 36 (2000) 884–890. <https://doi.org/10.1007/BF02758698>

[81] Y. Ohshita, Reactants in SiC chemical vapor deposition using CH_3SiH_3 as a source gas, J. Cryst. Growth 147 (1995) 111–116. [https://doi.org/10.1016/0022-0248\(94\)00656-3](https://doi.org/10.1016/0022-0248(94)00656-3)

[82] C.W. Liu, J.C. Sturm, Low temperature chemical vapor deposition growth of β -SiC on (100) Si using methylsilane and device characteristics, J. Appl. Phys. 82 (1997) 4558–4565. <https://doi.org/10.1063/1.366192>

[83] I. Golecki, F. Reidinger, J. Marti, Single-crystalline, epitaxial cubic SiC films grown on (100) Si at 750 °C by chemical vapor deposition, Appl. Phys. Lett. 60 (1992) 1703–1705. <https://doi.org/10.1063/1.107191>

- [84] E. Scalise, A. Marzegalli, F. Montalenti, L. Miglio, Temperature-dependent stability of polytypes and stacking faults in Si C: Reconciling theory and experiments *Physical Review Applied*, 12 (2019) 021002. <https://doi.org/10.1103/PhysRevApplied.12.021002>
- [85] N. Pangarov, The crystal orientation of electrodeposited metals, *Electrochimica Acta* 7 (1962),139-146. [https://doi.org/10.1016/0013-4686\(62\)80023-1](https://doi.org/10.1016/0013-4686(62)80023-1)
- [86] N. Pangarov, On the crystal orientation of electrodeposited metals, *Electrochim. Acta* 9 (1964) 721–726. [https://doi.org/10.1016/0013-4686\(64\)80060-8](https://doi.org/10.1016/0013-4686(64)80060-8)

Nomenclature and abbreviations

BF: bright field (TEM images)

CDD: coherent diffracting domain

CD1: one of the three alternate CVD SiC coatings (see [Table 1](#))

CD2: one of the three alternate CVD SiC coatings (see [Table 1](#))

CR: one of the two “regular” CVD SiC coatings (see [Table 1](#))

CVD: chemical vapor deposition

CVI: chemical vapor infiltration

CW: column width

DF: dark field (TEM images)

FFD: fault-free domains

HRTEM: High-resolution TEM

ID: Ising domains (faulted domains)

IFFT: inverse fast Fourier transform

MD: one of the three alternate CVD SiC coatings (see [Table 1](#))

MR: one of the two “regular” CVD SiC coatings (see [Table 1](#))

ODD: one-dimensionally-disordered (SiC)

RMS: Raman micro-spectroscopy

SAD: selected area diffraction

SF: stacking fault

SFD: stacking fault density

TEM: transmission electron microscopy

X: axis of the laboratory and incident laser light propagation direction

XRD: X-ray diffraction

Y: axis of the laboratory perpendicular to *X* axis and oriented vertically with respect to the cross-section of the specimen being analyzed. Also one of the two polarization directions of the scattered light (along *Y* axis of the laboratory)

Y: growth direction of the coating (along *Y* axis of the laboratory)

Y+Z: no polarization of the scattered light

Z: axis of the laboratory perpendicular to *X* and *Y* axes, and oriented horizontally with respect to the cross-section of the specimen being analyzed. Also one of the two polarization directions of the scattered light (along *Z* axis of the laboratory)

Z: growth direction of the coating (along *Z* axis of the laboratory)

Δ TO: transverse optical Raman peak splitting TO_1 - TO_2 [19,52] (here $E_1(TO)$ - $A_1(TO)$ / E_{2high})

θ : X-ray diffraction angle

(*hkl*): crystallographic planes

{*hkl*}: family crystallographic plane

<*hkl*>: family of crystallographic directions

<**YYZ**>: example of polarization/specimen orientation arrangements during Raman analyses (here: *Y* = incident light polarization direction, **Y** = growth direction of the coating and *Z* = scattered light polarization direction)

Figure captions

Fig. 1: Detail of the XRD diagrams showing the (111) peak and stacking fault features at the bottom of the (111) peak. The intensity of the (111) peak is normalized for all coatings. Insert: the normalized intensity is multiplied by 10 for CR, CD1 and MR, and the patterns are vertically shifted for better viewing of the stacking fault features

Fig. 2: Raman spectra of the various CVD SiC coatings

Fig. 3: Raman spectra of the various CVD SiC coatings in different polarization/orientation configurations. CR (a), CD1 (b), MR (c), CD2 (d) and MD (e) coatings

Fig. 4: Low magnification BF images of the CR (a) and MR (b) coatings

Fig. 5: DF images and SAD patterns of the CR (a) and MR (b) coatings (the SAD patterns are indexed along the [-110] zone axis). The dotted black circle determines the position of the selected area for diffraction, the white box marks the area of the HRTEM image shown in Fig. 6. The spots pointed by the symbol # are attributed either to twinning along {111} planes or an α polytype.

Fig. 6: HRTEM images (with detail and associated Fourier Transform) for CR (a) and MR (b) coatings (the SAD patterns are indexed along the [-110] (a) and [1000] (b) zone axes, respectively). The Fourier Transforms are calculated from the dotted black box area on HRTEM images

Fig. 7: TEM micrographs of the CD1 coating. Low magnification DF image (a), SAD pattern (b), and HRTEM images (c, d). On DF image, the dotted black circle determines the position of the selected area for diffraction, the white box marks the area of the HRTEM image

Fig. 8: TEM analysis of CD2 coating. DF images (a) and (b), associated SAD patterns (c) and (d) indexed along respectively the [-1,-1,2] and [-1,1,0] zone axis. On DF image, the dotted white circle determines the position of the selected area for diffraction

Fig. 9: TEM analysis of the MD coating. DF image (a), SAD pattern (b), and HRTEM images (c,d). On DF image, the dotted white circle determines the position of the selected area for diffraction, the white box marks the area of the HRTEM image

Fig. 10: Structural defects in CD2 coating. BF image of the surface of the coating (a), magnification in the stacking fault area (arrows indicate SF annulations) (b), HRTEM image of a mottled area (c), IFFTs with the (111) frequencies of a detail (d) (“T” marks indicate dislocation). On BF image, long dotted black box marks the magnification of SF area, short dotted black box locates the HR image of the mottled area

Figures

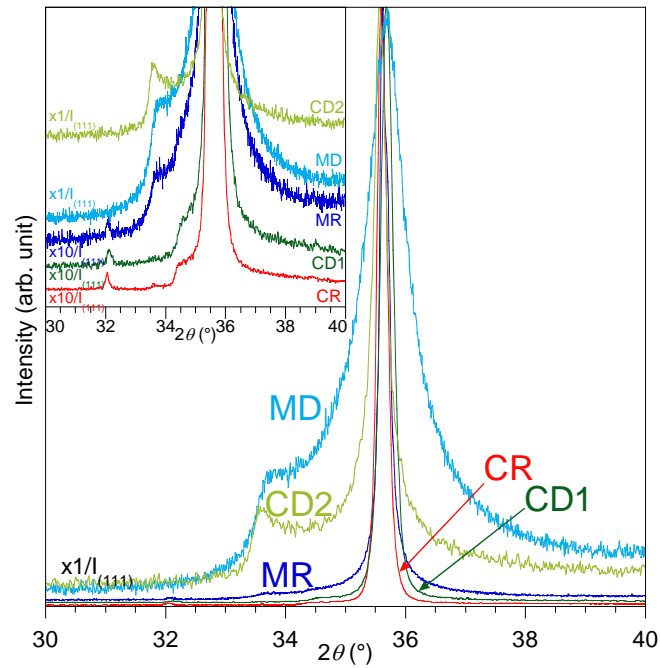


Fig. 1: Detail of the XRD diagrams showing the (111) peak and stacking fault features at the bottom of the (111) peak. The intensity of the (111) peak is normalized for all coatings. Insert: the normalized intensity is multiplied by 10 for CR, CD1 and MR, and the patterns are vertically shifted for better viewing of the stacking fault features

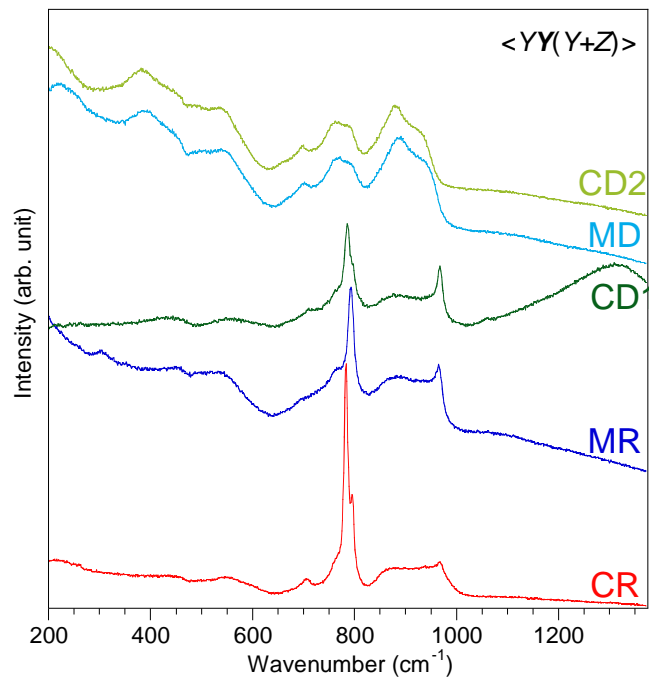


Fig. 2: Raman spectra of the various CVD SiC coatings

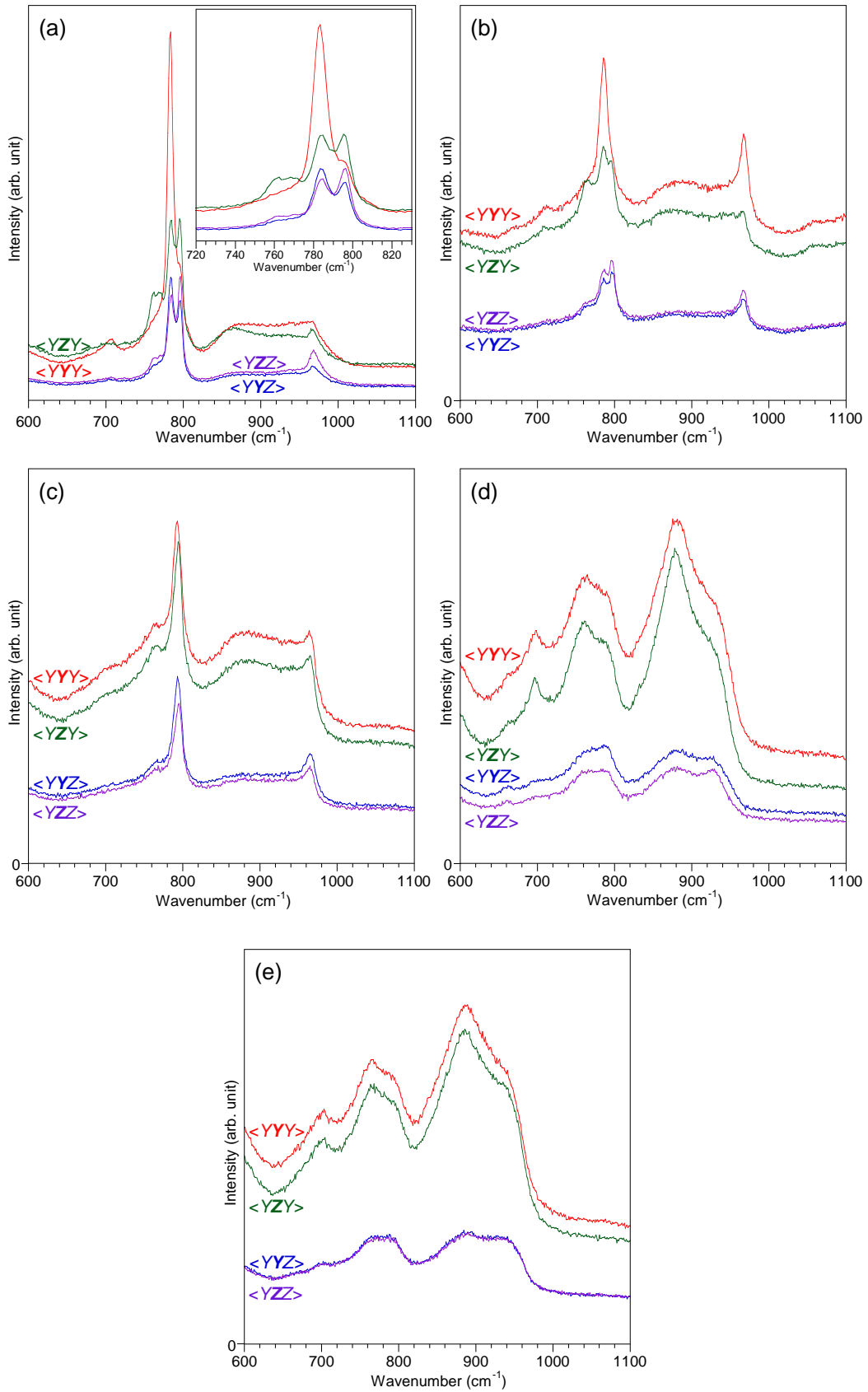


Fig. 3: Raman spectra of the various CVD SiC coatings in different polarization/orientation configurations. CR (a), CD1 (b), MR (c), CD2 (d) and MD (e) coatings

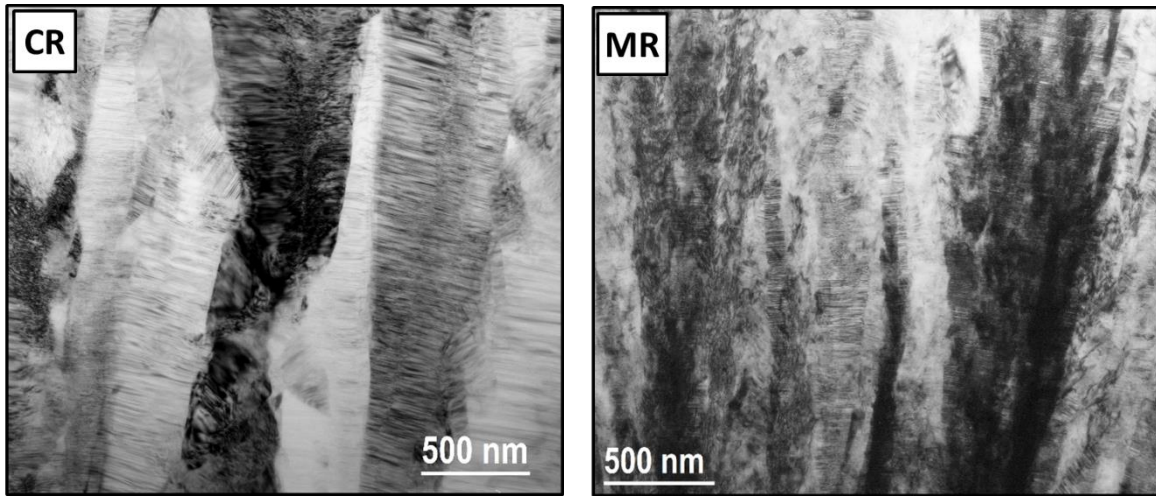


Fig. 4: Low magnification BF images of the CR (a) and MR (b) coatings

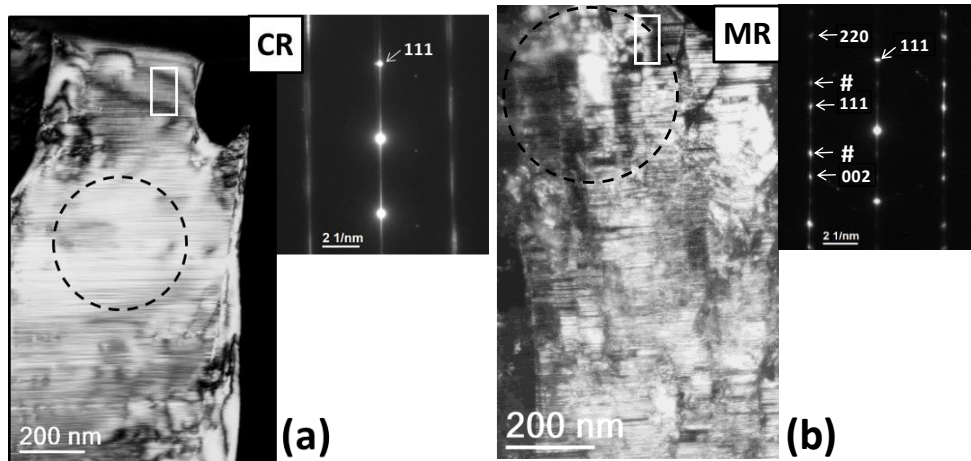


Fig. 5: DF images and SAD patterns of the CR (a) and MR (b) coatings (the SAD patterns are indexed along the $[-110]$ zone axis). The dotted black circle determines the position of the selected area for diffraction, the white box marks the area of the HRTEM image shown in Fig. 6. The spots pointed by the symbol # are attributed either to twinning along $\{111\}$ planes or an α polytype.

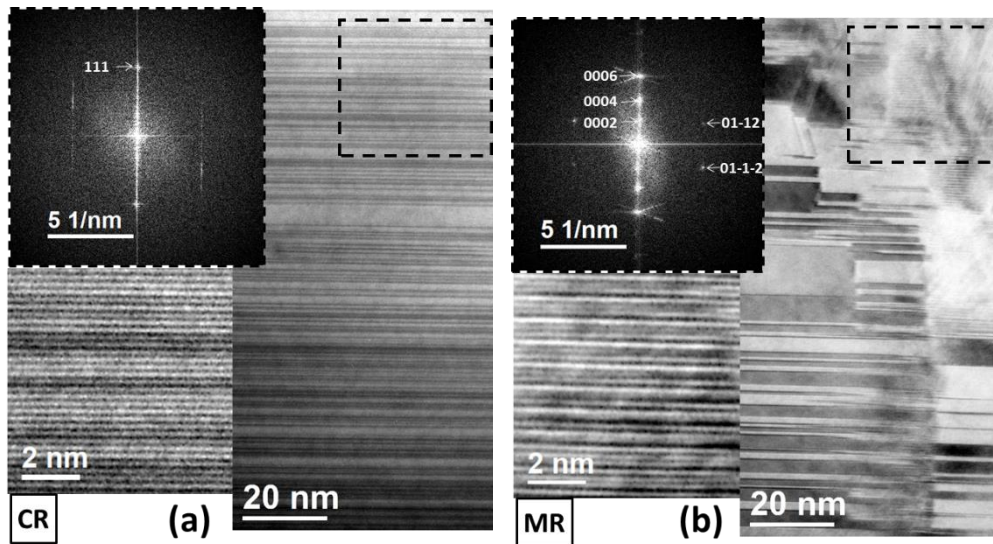


Fig. 6: HRTEM images (with detail and associated Fourier Transform) for CR (a) and MR (b) coatings (the SAD patterns are indexed along the $[-110]$ (a) and $[1000]$ (b) zone axes, respectively). The Fourier Transforms are calculated from the dotted black box area on HRTEM images

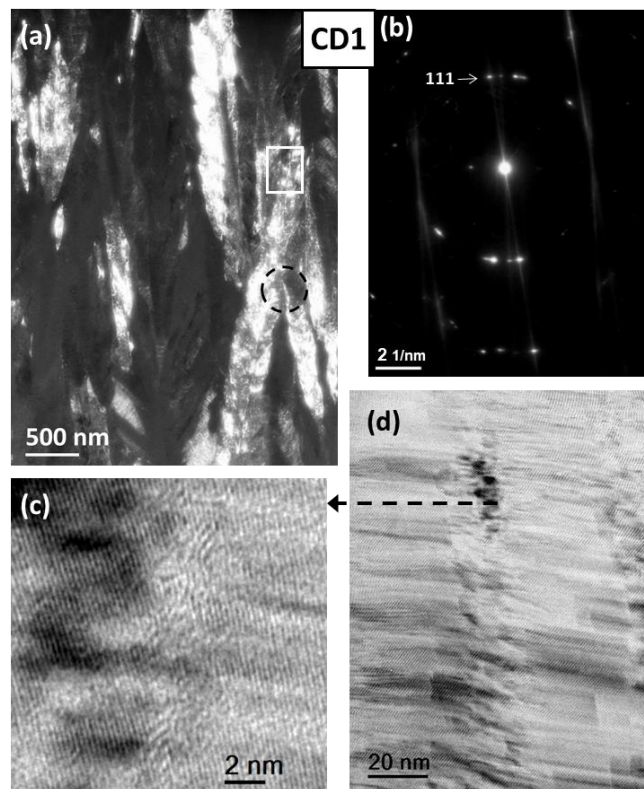


Fig. 7: TEM micrographs of the CD1 coating. Low magnification DF image (a), SAD pattern (b), and HRTEM images (c, d). On DF image, the dotted black circle determines the position of the selected area for diffraction, the white box marks the area of the HRTEM image

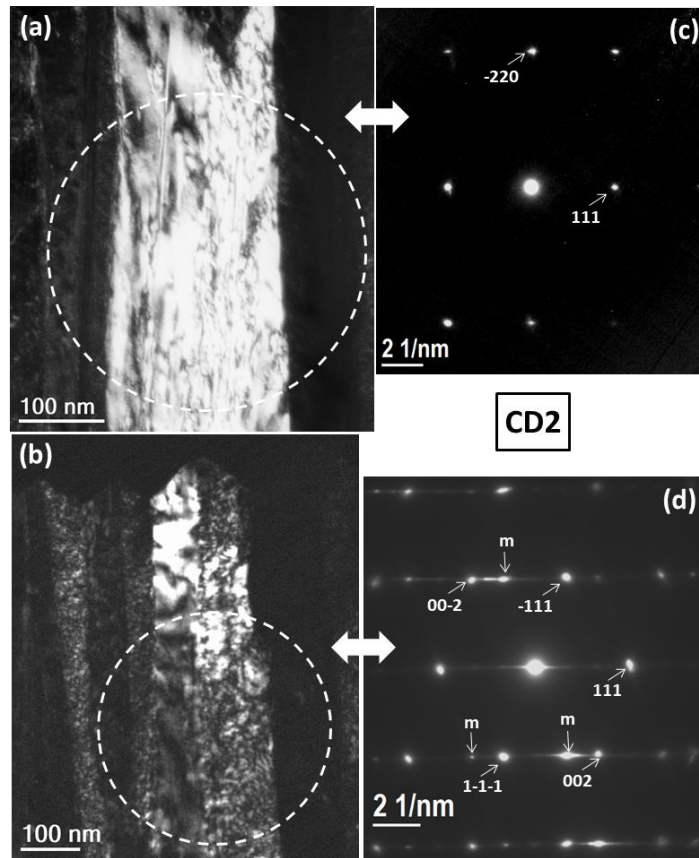


Fig. 8: TEM analysis of CD2 coating. DF images (a) and (b), associated SAD patterns (c) and (d) indexed along respectively the $[-1,-1,2]$ and $[-1,1,0]$ zone axis. On DF image, the dotted white circle determines the position of the selected area for diffraction

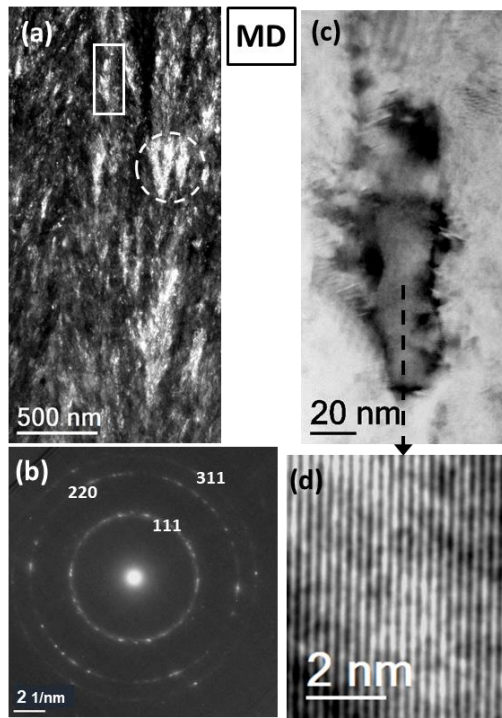


Fig. 9: TEM analysis of the MD coating. DF image (a), SAD pattern (b), and HRTEM images (c,d). On DF image, the dotted white circle determines the position of the selected area for diffraction, the white box marks the area of the HRTEM image

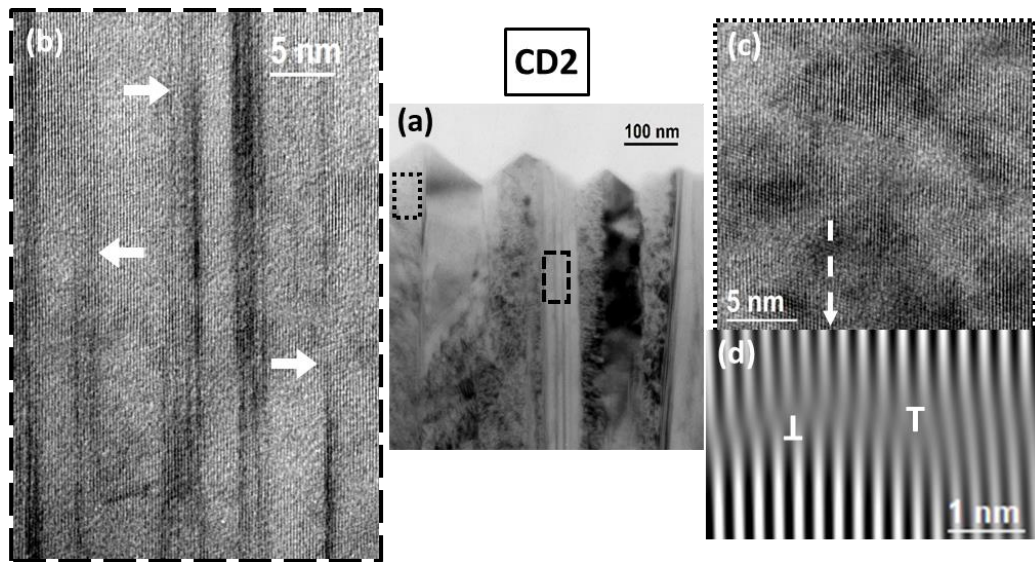


Fig. 10: Structural defects in CD2 coating. BF image of the surface of the coating (a), magnification in the stacking fault area (arrows indicate SF annulations) (b), HRTEM image of a mottled area (c), IFFTs with the (111) frequencies of a detail (d) (“T” marks indicate

dislocation). On BF image, long dotted black box marks the magnification of SF area, short dotted black box locates the HR image of the mottled area.